Twin stars as probes of the nuclear equation of state: Effects of rotation through the PSR J0952-0607 pulsar and constraints via the tidal deformability from the GW170817 event

Lazaros Tsaloukidis[*]

Max Planck Institute for the Physics of Complex Systems (MPI-PKS) and Würzburg-Dresden Cluster of Excellence ct.qmat, 01187 Dresden, Germany

P. S. Koliogiannis,[†] A. Kanakis-Pegios,[‡] and Ch. C. Moustakidis[§]

Department of Theoretical Physics, Aristotle University of Thessaloniki, 54124 Thessaloniki, Greece

(Received 27 October 2022; accepted 16 December 2022; published 17 January 2023)

In agreement with the constantly increasing gravitational wave events, new aspects of the internal structure of compact stars can be considered. A scenario in which a first-order transition takes place inside these stars is of particular interest, as it can lead, under certain conditions, to a third gravitationally stable branch (besides white dwarfs and neutron stars), the twin stars. The new branch yields stars with the same mass as normal compact stars but quite different radii. We focus on hybrid stars undergoing a hadron-to-quark phase transition near their core and how this new stable configuration arises. Emphasis is given on the aspects of the phase transition and its parametrization in two different ways—namely, with the Maxwell and Gibbs constructions. We systematically study the gravitational mass, the radius, and the tidal deformability, and we compare them with the predictions of the recent observation by the LIGO/VIRGO Collaboration, the GW170817 event, and the mass and radius limits, suggesting possible robust constraints. Moreover, we extend the study to include rotation effects on the twin star configurations. The recent discovery of the fast rotating supermassive pulsar PSR J0952-0607 triggered the efforts to constrain the equation of state and, moreover, to examine possible predictions related to the phase transition in dense nuclear matter. We pay special attention to relate the PSR J0952-0607 pulsar properties to the twin star predictions, and mainly to explore the possibility that the existence of such a massive object would rule out the existence of twin stars. Finally, we discuss the constraints on the radius and mass of the recently observed compact object within the supernova remnant HESS J1731-347. The estimations imply that this object is either the lightest known neutron star or a star with a more exotic equation of state.

DOI: 10.1103/PhysRevD.107.023012

I. INTRODUCTION

Compact stars yield the most prominent natural laboratories for the study of exotic forms of matter [1–4]. Recently discovered pulsars alongside gravitational wave detection, such as GW170817, have revealed new aspects of the internal structure of these stars, mainly in terms of their composition [5–7]. While the equation of state (EOS) of nuclear matter is well established up to nuclear saturation density, one encounters the challenge of describing matter in fairly higher densities realized in the interior of these stars. At these densities the type of matter is yet to be determined, and, in turn, the ability to construct stellar models that agree with the aforementioned observations is still an open issue. Possible candidates are pure neutron stars composed of hadrons, strange quark stars composed of deconfined quarks, and hybrid stars composed of hadronic outer shells and cores of deconfined quarks. In this article the final case is claimed.

Stars of this branch are expected to have masses in the same range as normal neutron stars, yet with fairly small radii. The existence of such stars is a strong indication that a hadron-quark phase transition (HQPT) is a physical reality, a result of utmost importance, especially in the study of dense matter physics [8–11]. A study of the HQPT is presented here, where the conditions under which the twin star configuration arises are examined. The compatibility of the mass and radius constraints, as they are formed through up-to-date observations, is also considered.

The idea of a third family of compact stars and, in particular, the connection with the possibility of its being a signature of a strong phase transition in the interior of the star, was first introduced by Gerlach [12]. Later, Kämpfer

[*]ltsalouk@pks.mpg.de
[†]pkoliogi@physics.auth.gr
[‡]alkanaki@auth.gr
[§]moustaki@auth.gr

worked also on this issue [13,14]. Glendenning and Kettner introduced the term "twins" in their paper [15], while at the same time Schertler *et al.* [16] worked out the idea in detail. However, in all previous studies, the maximum mass was approximately at the canonical binary pulsar mass $1.4M_\odot$. The revival of the idea of twin stars was started a few years later by Blaschke *et al.* [17,18]. Specifically, in the aforementioned papers it is suggested that high-mass twin stars, once detected by simultaneous mass and radius measurements, could provide evidence for a strong first-order phase transition in cold matter, which then would imply the existence of at least one critical end point in the quantum chromodynamics phase diagram. Moreover, in the same work examples of EOSs are also presented, for the first time, that would not only provide twin solutions but also fulfill the constraint on the maximum mass from the existence of pulsars as heavy as $2M_\odot$ [17,18]. This idea was elaborated on by Benic *et al.* [19] (see also Ref. [20]). A systematic Bayesian analysis of the new twin star EOS with observational constraints was presented in Ref. [21]. Finally, analyses of the robustness of twin solutions against changing the Maxwell to a mixed phase construction and the formation of structures in the mixed phase due to the interplay of the surface tension and Coulomb interaction effects were considered in Refs. [22,23], respectively. Some recent works dedicated to the study of phase transitions in the interior of the neutron stars and the possible existence of twin stars include Refs. [24–66].

Pulsar PSR J0952-0607 was first discovered by Bassa *et al.* [67]. It has a frequency of $f = 709$ Hz, making it the fastest known spinning pulsar in the disk of the Milky Way. Very recently, Romani *et al.* [68] discovered that PSR J0952-0607 has a mass of $M = 2.35 \pm 0.17M_\odot$, which is the largest well measured mass found to date. The above discoveries triggered research into the constraints of the EOS of dense nuclear matter and is likely to revise many of the theoretical predictions concerning the basic properties of neutron stars (for a recent study, see Ref. [69]). One of them is the existence of twin stars, which is the main subject of this study. In particular, the existence of a supermassive neutron star may rule out twin stars (see Ref. [28]). In this sense, observation of such supermassive stars is decisive for checking the reliability of the corresponding theoretical predictions, and therefore a systematically and careful analysis should be considered. On the other hand, theoretical calculations for the maximum possible mass of neutron stars should be combined with recent observations concerning the radius and tidal deformability of stars with a mass close to $1.4M_\odot$. In general, a nuclear model can be judged by its flexibility in being able to predict the maximum possible mass while correctly estimating the observational radial and tidal deformability values.

Moreover, one of the motivations for this work is to examine in a more systematic way the applications of the two main formulations of the phase transition, that is, the Maxwell construction (MC) and the Gibbs construction (GC). These formulations are quite different, as the former imposes an energy jump between the two phases, while the latter implements a smooth transition between the phases. It is worth mentioning that although the MC has been extensively applied in the literature, the GC has not received the attention it deserves (for a recent relevant study, see Ref. [11]). In any case, a comparison of their predictions may offer useful physical insights.

Rotating neutron stars with exotic degrees of freedom in their cores have already been studied in limited papers by Banik *et al.* [60], Bhattacharyya *et al.* [43], Haensel *et al.* [63], and Bozzola *et al.* [64]. In this study, in addition to the aforementioned similar studies, the effects of rapid rotation on the twin stars scenario are explored. The reason for this kind of study is twofold: On the one hand, we intend to examine to what extent high rotation can differentiate the representation of the two stability branches of a static neutron star. On the other hand, we want to consider the possible cases where the existence of the twin stars may have arisen as a result of the high rotational frequency, where in the corresponding static case such a scenario is not foreseen. To our knowledge, this peculiar case has not been explored in detail in the relevant literature, at least thus far. There is only an interesting mention in Ref. [60]. Nonetheless, future study is in progress in order to further clarify the effects of rotation on the twin star problem.

Finally, we employ the constraints on the mass and radius of the recently observed compact object within the supernova remnant HESS J1731-347 [70]. The corresponding estimations are $M = 0.77^{+0.20}_{-0.17}M_\odot$ and $R = 10.4^{+0.86}_{-0.78}$ km, respectively, while the observations were carried out with the help of modeling of the x-ray spectrum and a robust distance estimate from *Gaia* observations [70]. According to Doroshenko *et al.*'s guess, the above estimates imply that this object is either the lightest neutron star known or a star with a more exotic equation of state. In any case, it is worth considering to what extent this compact object is compatible with the hybrid model, and thus with the twin star theory.

The paper is organized as follows. In Sec. II we present the basic formalism of the hadron-to-quark phase transition, while in Sec. III we provide the tidal deformability. Section IV is dedicated to the presentation and discussion of the results of this study, while our concluding remarks are given in Sec. V.

II. HADRONIC-TO-QUARK MATTER PHASE TRANSITION

A. Hybrid EOS and first-order phase transition

The theoretical framework throughout this work is based on the two prescriptions for matching the low to intermediate density hadronic EOS to the one describing the free quark matter, the Maxwell and Gibbs constructions

(for an extensive and insightful analysis, see the recent review in Ref. [8]). In particular, while both methods have a phenomenological origin, they mimic, in a way, the theoretical approach of the phase transition. It is important to note that neither of these constructions take into account finite-size effects in the theory, so there are no surface or Coulomb term contributions present. In this sense, they should be considered a useful mathematical tool rather than an exact description of the phase transition from hadronic to free quark matter. Furthermore, although the MC appears to be more applicable, recent observations of gravitational waves related to the binary neutron star merger GW170817 event, along with the flexibility of the GC, have made the latter case a more compelling candidate [11]. Nevertheless, both methods have been used in the literature, leading under certain circumstances to the appearance of twin stars.

We note here that, as the quark phase has a strong dependence on the speed of sound, for both configurations, in order to achieve the observed neutron star masses. At the selected transition densities, the speed of sound is set equal to the speed of light, having as a result the maximally stiff EOS.

1. Maxwell construction

The first case is the well-known MC case, which exhibits a sharp transition at the boundary and makes it difficult for charged clusters of quarks to form in the hadronic matter. This construction is the favored one, in the case where the surface tension σ_s in the hadron-quark crossover is higher than the critical value of ≈ 40 MeV fm^{-3} and less than the maximum allowed one of ≈ 100 MeV fm^{-3}, according to QCD lattice gauge simulations, with its exact value highly uncertain [71]. Of course, as expected, an abrupt phase change of this kind yields a discontinuity in at least one physical quantity, with the most obvious one, the energy density, having the form [9–11]

$$\mathcal{E}(P) = \begin{cases} \mathcal{E}_{\rm hadron}(P), & P \le P_{\rm tr} \\ \mathcal{E}(P_{\rm tr}) + \Delta\mathcal{E} + c_s^{-2}(P - P_{\rm tr}), & P > P_{\rm tr}. \end{cases} \quad (1)$$

In Eq. (1) $\mathcal{E}(P)$ denotes the energy density, P the pressure, $c_{\rm s} = \sqrt{\partial P/\partial \mathcal{E}}$ the speed of sound in units of the speed of light, and $\Delta\mathcal{E}$ the magnitude of the energy density jump at the transition point. During the quark phase the numerical value we assign for $c_{\rm s}$ is equal to $c_s = 1$, the maximum allowed value that is consistent with causality. That way, we also ensure the stiffest EOS case and the greatest possible maximum mass in the resulting M-R diagram. Moreover, $P_{\rm tr}$ expresses the pressure that corresponds to the baryon density at the phase transition point, $n_{\rm tr}$. It should be clear that the first line in Eq. (1) refers to the hadronic phase, while the second one refers to the quark phase, seen as the first-order Taylor expansion of the energy density around the transition pressure plus the $\Delta\mathcal{E}$ term. This is the so-called constant speed of sound (CSS) parametrization [9,11,72–74]. The described process requires not only the pressure but also the rest of the intensive thermodynamic quantities, meaning that the temperature T (set equal to 0) and the baryonic chemical potential $\mu_{\rm B}$ of both phases have the same value at the phase transition. The same is not true for the electric chemical potential $\mu_{\rm Q}$, as there is a jump at the interface between the two phases [26]. Local charge neutrality conditions for both regions must separately be imposed in order to ensure a β-equilibrium state.

2. Gibbs construction

In the case of a nonsharp HQPT, meaning very low values of the surface tension σ_s, a finite region to embody the transition is implied. The mixed phase of this transition is composed, as its name suggests, of intermittent domains of pure hadronic and quark phases [11,26]. The Gibbs phase transition rule regarding the equality of the pressure of the two components (the hadron-intermediate and intermediate-quark ones) is established here. Constraints requiring global charge neutrality and baryon conservation number are imposed throughout the process, meaning that both the baryon and electric chemical potentials, $\mu_{\rm B}$ and $\mu_{\rm Q}$, are required to have the same value across the phase boundaries. This is quite important, as now both phases can be oppositely charged, as long as the mixed phase remains neutrally charged. In this case it is only logical that nuclear matter is positively charged, assuming an equal number of protons and neutrons (minimizing nuclear asymmetry energy), while, to compensate, quark matter, on the other hand, has to be negatively charged. Contrary to the MC case, where the pressure remains constant in the transition interval, in the GC case the pressure increases with increasing baryon density, while also no discontinuities in the energy density appear, giving rise to the profile [11]

$$\mathcal{E}(P) = \begin{cases} \mathcal{E}_{\rm hadron}(P), & P \le P_{\rm tr}, \\ A_{\rm m}(P/K_{\rm m})^{1/\Gamma_{\rm m}} + \gamma_{\rm m} P, & P_{\rm tr} \le P \le P_{\rm CSS}, \\ \mathcal{E}(P_{\rm CSS}) + c_s^{-2}(P - P_{\rm CSS}), & P \ge P_{\rm CSS}, \end{cases} \quad (2)$$

where $A_{\rm m} = 1 + \alpha_{\rm m}$, $\gamma_{\rm m} = (\Gamma_{\rm m} - 1)^{-1}$, and $c_{\rm s} = 1$ (maximally stiff EOS). The energy density is denoted by $\mathcal{E}(P)$, the pressure by P, and the speed of sound by $c_{\rm s}$, while a_m, K_m, and the polytropic index Γ_m are constants, with the first two evaluated by requiring the continuity of P and $\mathcal{E}$ at the transition points. As already explained, an energy density jump is not present here, as opposed to the MC, but the increase in the quantity is assigned during the intermediate part of the formula. The subscript "CSS" denotes the corresponding quantity at the start of the quark phase. That being said, it should be understood that discontinuities in the derivatives of the pressure with regard to the energy

density are still present here at the points where the mixed phase begins and ends. This is clearly reflected in the value of the speed of sound c_s between the three phases.

The relation between the pressure and baryon density for the intermediate section in Eq. (2) is given through the well-known, simple polytropic formula $P(n) = K_m n^{\Gamma_m}$. While the values of a_m and K_m depend on the transition point, the polytropic index Γ_m in the GC is taken to be constant throughout the work and is equal to 1.03. A value so close to unity is justified by taking into account the uncertainty related to how soft the EOS of the mixed phase is and also differentiating it as much as possible from the respective value of the MC, where, according to the relevant discussion above, we have $\Gamma_m = 0$ (see also Ref. [11]).

B. Seidov criterion

In general, the phase transition from hadronic to quark matter described in the previous section is not sufficient by itself to predict the existence of a third family of compact stars. To be more specific, this existence requires, in the corresponding mass-radius diagram, the appearance of an unstable region followed by a stable one (for an instructive discussion, see Ref. [3]). The criterion for causing an unstable region by a first-order phase transition in neutron stars was first considered by Seidov [75]. His work was based on the work of Lighthill [76], who performed a linear perturbative expansion on the size of the quark matter core.

In particular, we consider an EOS and a phase transition at the pressure $P_{\rm tr}$ which corresponds to the energy density $\mathcal{E}_1 \equiv \mathcal{E}_{\rm tr}$, with a simultaneous jump to the energy density $\mathcal{E}_2 \equiv \mathcal{E}(P_{\rm tr}) + \Delta\mathcal{E}$. In general, a stable sequence where the mass increases with the central pressure will become an unstable one as the mass decreases with the central pressure. This case takes place only if the following inequality holds [3]:

$$3P_{\rm tr} + 3\mathcal{E}_1 - 2\mathcal{E}_2 < 0.$$

Thus, we finally find the minimum jump in the energy density that is required for the appearance of an unstable configuration and which is given by the relation

$$\Delta\mathcal{E}_{\rm cr} = \frac{1}{2}\mathcal{E}_{\rm tr} + \frac{3}{2}P_{\rm tr}. \tag{3}$$

In order to have a third family of compact objects appear in the $M - R$ diagram, the aforementioned instability has to be satisfied. The theory dictates that as long as the mass M is an increasing function of the central pressure P_c, the star will remain stable. As the central pressure increases, it reaches a certain point where its value becomes equal to the transition pressure $P_{\rm tr}$, leading to the formation of the quark matter core. Depending on whether or not the Seidov criterion for the energy density jump is surpassed, there are four possible outcomes, with only two of them producing a new type of compact object [3,9]. It should be noted here that the Seidov criterion is meaningful only in the presence of a sharp discontinuity in the energy density profile, which appears in the MC method as opposed to the GC method.

In order to be able to compare the GC with the MC, where an energy jump appears in the form of $\Delta\mathcal{E}_{\rm cr}$, we define the corresponding energy increase in the GC as the quantity

$$\Delta\mathcal{E}_{\rm G} = \frac{3}{2}\left(\frac{1}{2}\mathcal{E}_{\rm hadron}(P_{\rm tr}) + \frac{3}{2}P_{\rm tr}\right), \tag{4}$$

with $\mathcal{E}_{\rm hadron}(P_{\rm tr})$ and $P_{\rm tr}$ representing the respective values at the transition from the hadron phase to the mixed phase.

The two possible outcomes for producing a new type of compact objects are now briefly described. Case 1: If $\Delta\mathcal{E}$ is taken to be much higher than the Seidov limit ($\Delta\mathcal{E} \gg \Delta\mathcal{E}_{\rm cr}$), then the instability appears immediately after the formation of the quark matter core. In the M-R diagram, the transition point takes the form of a cusp, meaning the sign of dM/dR is flipped. This case does not result in the formation of a stable hybrid star (see the case $n_{\rm tr} = 0.5$ fm^{-3} in Fig. 3). Case 2: The value of $\Delta\mathcal{E}$ should be higher that the value of Eq. (3) ($\Delta\mathcal{E} > \Delta\mathcal{E}_{\rm cr}$), but not high enough to reach the case 1 scenario. This case describes the appearance of a third family of compact objects. The cusp is also present here during the transition point, leading to an unstable disconnected area in the graph, which after a while flips around again, signaling the appearance of a stable hybrid star with a quark matter core.

In this work we also study two cases where the Seidov criterion is violated (for more details, see Chap. 9 of Ref. [3] and Fig. 3 in Ref. [9]). They both include the hybrid branch connected to the nuclear star branch that may lead to the appearance of a third family of compact objects. These two cases are described below with their corresponding numbering as a continuation of the two previous cases. Case 3: The energy density jump $\Delta\mathcal{E}$ is not high enough to cause an instability at the moment ($\Delta\mathcal{E} < \Delta\mathcal{E}_{\rm cr}$), meaning that the quark matter is described by a curve on the map that is connected to the hadronic matter branch. The curve continues up to a point, after which an unstable region appears, leading again to a stable hybrid branch, as in the case 2 scenario, albeit shorter in length (see Fig. 12 for $n_{\rm tr} = 0.38$ fm^{-3}). Case 4: The hybrid star branch connected to the nuclear branch is also present here with its length to be inversely proportional to the ratio of $\Delta\mathcal{E}/\mathcal{E}_{\rm tr}$. It is shown that higher values of the above quantity lead to a decrease in the size of the hybrid branch that spans the phase diagram. Immediately after a maximum mass value is reached, a sudden discontinuity appears that continues forth without the appearance of a third family of compact objects [9].

III. TIDAL DEFORMABILITY

A very important source for the gravitational wave detectors is the gravitational waves from the late phase of the inspiral of a binary neutron star system before the merger [77–79]. This kind of source leads to the measurement of various properties of neutron stars. In the inspiral phase the tidal effects can be detected [78].

The k_2 parameter, also known as the tidal Love number, depends on the equation of state and describes the response of a neutron star to the tidal field E_{ij} [78]. The exact relation is

$$Q_{ij} = -\frac{2}{3} k_2 \frac{R^5}{G} E_{ij} \equiv -\lambda E_{ij}, \tag{5}$$

where R is the neutron star radius and $\lambda = 2R^5 k_2/3G$ is the tidal deformability. The tidal Love number k_2 is given by [78,79]

$$\begin{aligned} k_2 = {} & \frac{8\beta^5}{5}(1-2\beta)^2[2-y_R+(y_R-1)2\beta] \\ & \times [2\beta(6-3y_R+3\beta(5y_R-8)) \\ & + 4\beta^3(13-11y_R+\beta(3y_R-2)+2\beta^2(1+y_R)) \\ & + 3(1-2\beta)^2[2-y_R+2\beta(y_R-1)]\ln(1-2\beta)]^{-1}, \end{aligned} \tag{6}$$

where $\beta = GM/Rc^2$ is the compactness of a neutron star. The parameter y_R is determined by numerically solving the following differential equation:

$$r\frac{dy(r)}{dr} + y^2(r) + y(r)F(r) + r^2Q(r) = 0, \tag{7}$$

with the initial condition $y(0) = 2$ [80]. $F(r)$ and $Q(r)$ are functionals of the energy density $\mathcal{E}(r)$, pressure $P(r)$, and mass $M(r)$ defined as [77]

$$F(r) = \left[1 - \frac{4\pi r^2 G}{c^4}(\mathcal{E}(r) - P(r))\right]\left(1 - \frac{2M(r)G}{rc^2}\right)^{-1} \tag{8}$$

and

$$\begin{aligned} r^2Q(r) = {} & \frac{4\pi r^2 G}{c^4}\left[5\mathcal{E}(r) + 9P(r) + \frac{\mathcal{E}(r)+P(r)}{\partial P(r)/\partial \mathcal{E}(r)}\right] \\ & \times \left(1 - \frac{2M(r)G}{rc^2}\right)^{-1} - 6\left(1 - \frac{2M(r)G}{rc^2}\right)^{-1} \\ & - \frac{4M^2(r)G^2}{r^2c^4}\left(1 + \frac{4\pi r^3 P(r)}{M(r)c^2}\right)^2\left(1 - \frac{2M(r)G}{rc^2}\right)^{-2}. \end{aligned} \tag{9}$$

Equation (7) must be solved numerically and self-consistently with the Tolman-Oppenheimer-Volkoff (TOV) equations under the following boundary conditions: $y(0) = 2$, $P(0) = P_c$ (where P_c denotes the central pressure), and $M(0) = 0$ [77,79]. From the numerical solution of TOV equations, the mass M and radius R of the neutron star can be computed, while the corresponding solution of the differential equation (7) provides the value of $y_R = y(R)$. The last parameter along with the quantity β are the basic ingredients of the tidal Love number k_2.

The chirp mass $\mathcal{M}_c$ of a binary neutron star system is a well measured quantity by the gravitational wave detectors [7]. Its relation is given as

$$\mathcal{M}_c = \frac{(m_1 m_2)^{3/5}}{(m_1+m_2)^{1/5}} = m_1 \frac{q^{3/5}}{(1+q)^{1/5}}, \tag{10}$$

where m_1 is the mass of the heavier component star and m_2 is that of the lighter component star. Hence, the binary mass ratio $q = m_2/m_1$ lies within the range $0 < q \leq 1$.

Additionally, another quantity that is well measured is the effective tidal deformability $\tilde{\Lambda}$ which is given by [7]

$$\tilde{\Lambda} = \frac{16}{13}\frac{(12q+1)\Lambda_1 + (12+q)q^4\Lambda_2}{(1+q)^5}, \tag{11}$$

where Λ_i is the dimensionless tidal deformability [7],

$$\Lambda_i = \frac{2}{3}k_2\left(\frac{R_i c^2}{M_i G}\right)^5 \equiv \frac{2}{3}k_2\beta_i^{-5}, \qquad i = 1,2. \tag{12}$$

The effective tidal deformability $\tilde{\Lambda}$ is one of the main quantities that can be well measured by the detection of the corresponding gravitation waves.

IV. RESULTS

A. Mass vs radius diagram

In our study, as already mentioned, we have used two constructions, (a) the MC and (b) the GC, and two different EOSs, (a) the MDI + APR1 EOS [81] and (b) the GRDF-DD2 EOS [82]. Also, we have focused on the following values: $n_{\rm tr} = [0.20, 0.25, 0.30, 0.32, 0.35, 0.38, 0.43, 0.50]\,{\rm fm}^{-3}$. In Figs. 1–4 we show the $M-R$ diagrams for all cases. In particular, Figs. 1 and 2 indicate the MDI + APR1 EOS with the MC and the GC, respectively, while Figs. 3 and 4 show the GRDF-DD2 EOS with the MC and the GC, respectively. In each figure, panel (a) corresponds to $\Delta\mathcal{E}$ ($\Delta\mathcal{E}_{\rm cr}$ for the MC and $\Delta\mathcal{E}_{\rm G}$ for the GC) and panel (b) corresponds to the cases $\Delta\mathcal{E} = \Delta\mathcal{E}_{cr} + [100, 200]$ MeV fm^{-3} for the MC and $\Delta\mathcal{E} = \Delta\mathcal{E}_G + [100, 200]$ MeV fm^{-3} for the GC, respectively. A general remark is that the EOSs that fulfill the $\Delta\mathcal{E}_{\rm cr}$ ($\Delta\mathcal{E}_{\rm G}$) are stiffer than the cases with $\Delta\mathcal{E} = \Delta\mathcal{E}_{cr} + [100, 200]$ MeV fm^{-3} ($\Delta\mathcal{E} = \Delta\mathcal{E}_G + [100, 200]$ MeV fm^{-3}). Specifically, as we move to higher values of $\Delta\mathcal{E}$, the EOSs become softer (smaller high masses and smaller radii). The purple horizontal shaded regions correspond to observational data from the pulsars, while the

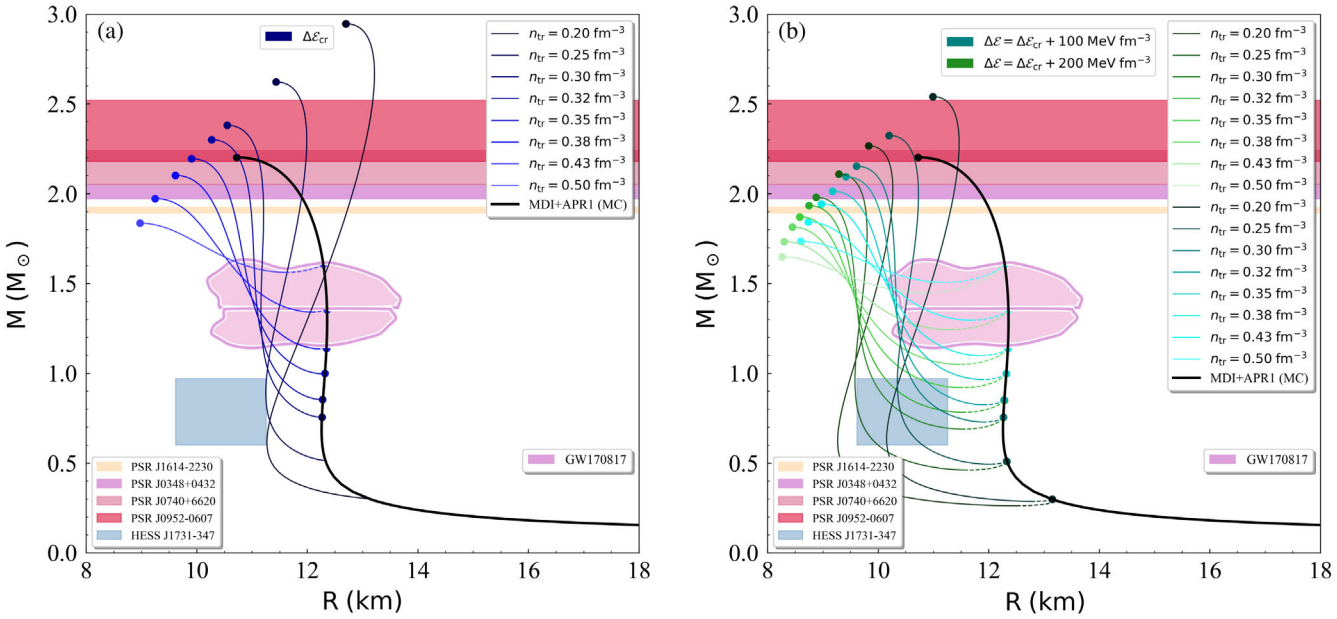

FIG. 1. Mass vs radius diagram for the MDI + APR1 EOS under the MC and for (a) $\Delta\mathcal{E}_{cr}$ and (b) $\Delta\mathcal{E} = \Delta\mathcal{E}_{cr} + 100$ MeV fm^{-3} (blue curves) and $\Delta\mathcal{E} = \Delta\mathcal{E}_{cr} + 200$ MeV fm^{-3} (green curves). The black curve indicates the original EOS. The shaded regions from bottom to top represent the HESS J1731-347 remnant [70], the GW170817 event [7], PSR J1614-2230 [83], PSR J0348 + 0432 [84], PSR J0740 + 6620 [85], and PSR J0952-0607 [68] pulsar observations for the possible maximum mass.

light purple contour shaded region indicates the observation of the GW170817 event [7]. The dashed part of the curves indicates their unstable region. Another remark is that between the two constructions, the MC and the GC, the first provides branches of EOSs in a lower mass region than the second. Therefore, the MC is more informative in our case of study since the GW170817 event contains low values for the component masses. Also, as one can observe, as we move to higher values of n_{tr} the EOSs become softer.

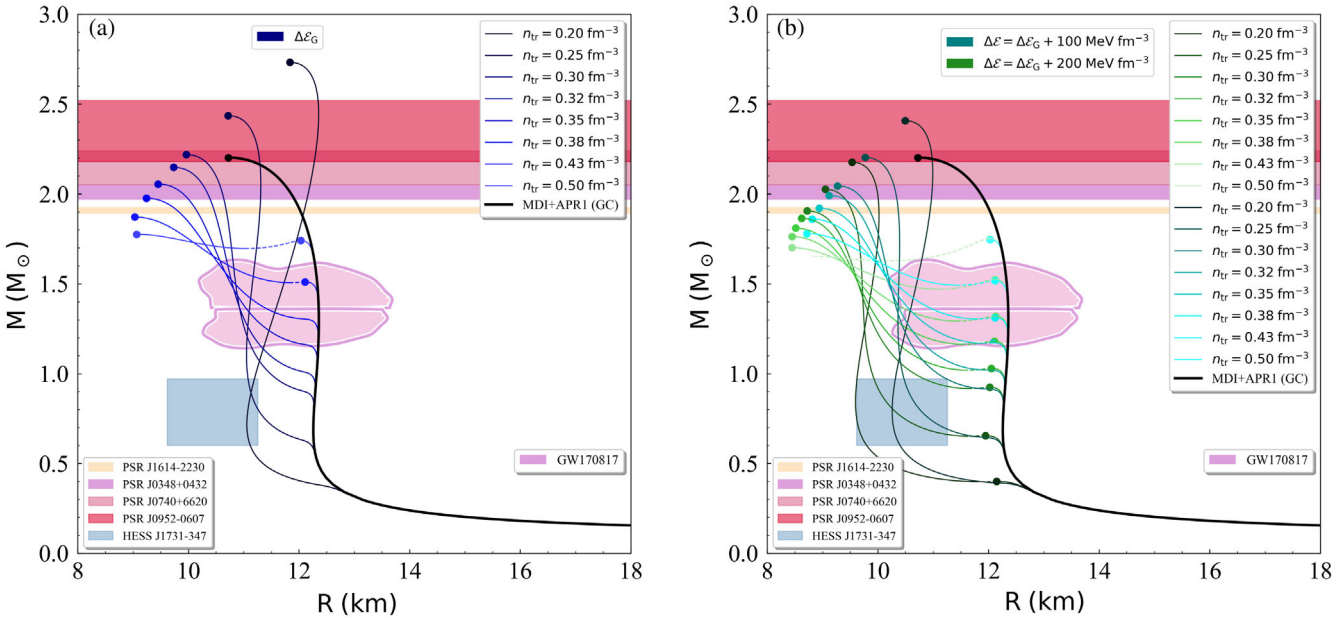

FIG. 2. Mass vs radius diagram for the MDI + APR1 EOS under the GC and for (a) $\Delta\mathcal{E}_G$ and (b) $\Delta\mathcal{E} = \Delta\mathcal{E}_G + 100$ MeV fm^{-3} (blue curves) and $\Delta\mathcal{E} = \Delta\mathcal{E}_G + 200$ MeV fm^{-3} (green curves). The black curve indicates the original EOS. The shaded regions from bottom to top represent the HESS J1731-347 remnant [70], the GW170817 event [7], PSR J1614-2230 [83], PSR J0348 + 0432 [84], PSR J0740 + 6620 [85], and PSR J0952-0607 [68] pulsar observations for the possible maximum mass.

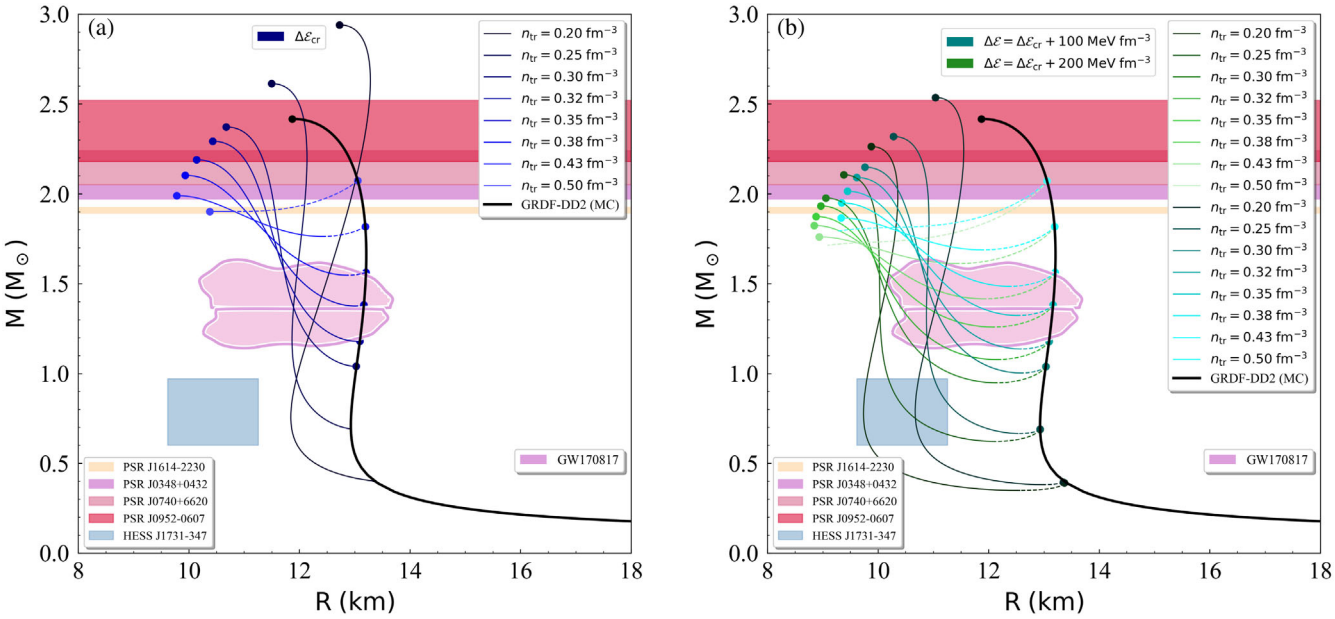

FIG. 3. Mass vs radius diagram for the GRDF-DD2 EOS under the MC and for (a) $\Delta\mathcal{E}_{cr}$ and (b) $\Delta\mathcal{E} = \Delta\mathcal{E}_{cr} + 100$ MeV fm^{-3} (blue curves) and $\Delta\mathcal{E} = \Delta\mathcal{E}_{cr} + 200$ MeV fm^{-3} (green curves). The black curve indicates the original EOS. The shaded regions from bottom to top represent the HESS J1731-347 remnant [70], the GW170817 event [7], PSR J1614-2230 [83], PSR J0348 + 0432 [84], PSR J0740 + 6620 [85], and PSR J0952-0607 [68] pulsar observations for the possible maximum mass.

Moreover, in Figs. 1–4, the constraints on the mass and radius of the recently observed remnant HESS J1731-347 have also been included [70]. Obviously, the prediction of the above constraints requires the use of a larger jump in the energy density for both constructions. In particular, we found that maybe this star is a hybrid star, belonging to the second stable branch. It is also remarkable that these predictions are compatible with the prediction of the maximum observed masses. It is worth mentioning that we do not claim that the remnant HESS J1731-347 is

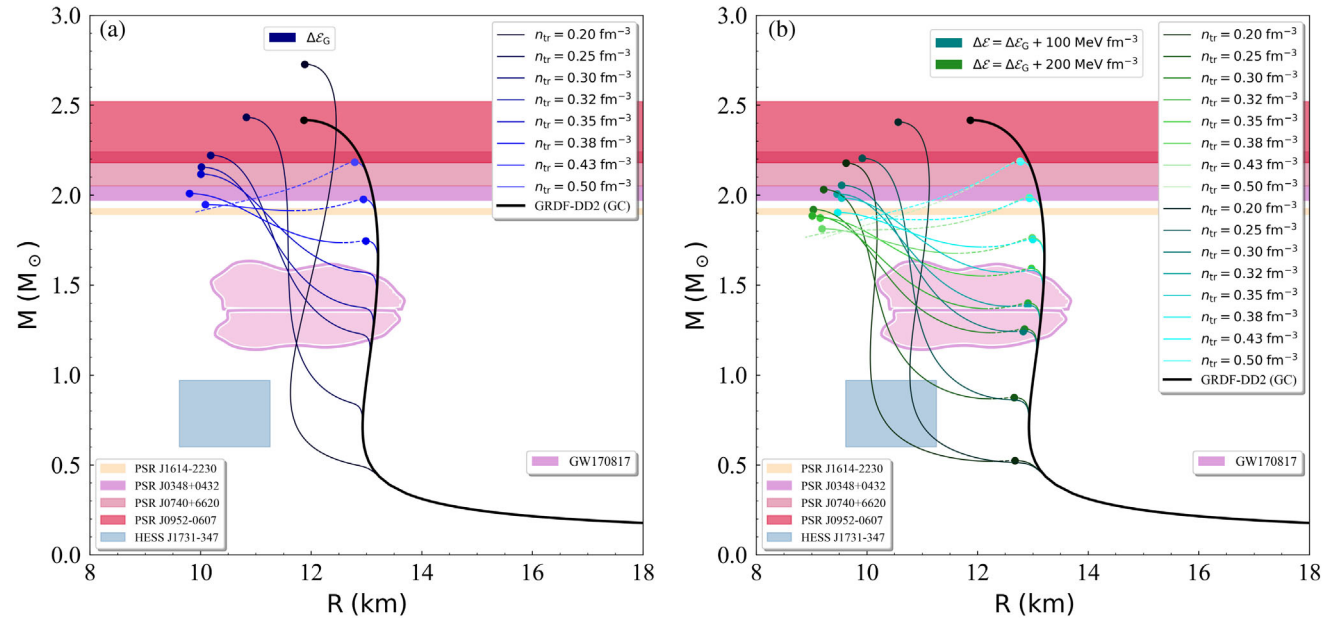

FIG. 4. Mass vs radius diagram for the GRDF-DD2 EOS under the GC and for (a) $\Delta\mathcal{E}_G$ and (b) $\Delta\mathcal{E} = \Delta\mathcal{E}_G + 100$ MeV fm^{-3} (blue curves) and $\Delta\mathcal{E} = \Delta\mathcal{E}_G + 200$ MeV fm^{-3} (green curves). The black curve indicates the original EOS. The shaded regions from bottom to top represent the HESS J1731-347 remnant [70], the GW170817 event [7], PSR J1614-2230 [83], PSR J0348 + 0432 [84], PSR J0740 + 6620 [85], and PSR J0952-0607 [68] pulsar observations for the possible maximum mass.

definitely a hybrid star. However, according to this study, this case is more favorable than the one with a neutron star. Further similar observations are needed in order to clarify this issue.

B. Tidal deformability

Figure 5 presents the tidal parameters k_2 and λ of a single neutron star as a function of its mass, for the MDI+APR1 EOS (MC) and for the cases with $\Delta\mathcal{E} = \Delta\mathcal{E}_{cr} + [100, 200]$ MeV fm^{-3}. The effect of the different $\Delta\mathcal{E}$ and $n_{\rm tr}$ can be observed, as they lead to distinct subbranches. In general, higher values of $\Delta\mathcal{E}$ lead to softer EOSs across the same bifurcation characterized by the value of the transition density $n_{\rm tr}$.

In Figs. 6 and 7 we present the $\Lambda_1 - \Lambda_2$ space for each EOS and configuration using the observational data of the GW170817 event (the orange shaded region) [7]. To be more specific, we considered the three following combinations: hybrid-hybrid binary star system (HS-HS), hybrid-neutron star system (HS-NS), and finally a neutron-neutron one (NS-NS). We notice that we concentrated only on the cases with $\Delta\mathcal{E} = \Delta\mathcal{E}_{cr} + [100, 200]$ MeV fm^{-3} for the MC and $\Delta\mathcal{E} = \Delta\mathcal{E}_{G} + [100, 200]$ MeV fm^{-3} for the GC, because these cases more easily provide a twin star branch on the EOS. The blue curves correspond to $\Delta\mathcal{E} = \Delta\mathcal{E}_{cr} +$ 100 MeV fm^{-3} ($\Delta\mathcal{E} = \Delta\mathcal{E}_{G} + 100$ MeV fm^{-3}) for the MC (the GC), while the green ones correspond to $\Delta\mathcal{E} = \Delta\mathcal{E}_{cr} +$ 200 MeV fm^{-3} ($\Delta\mathcal{E} = \Delta\mathcal{E}_{G} + 200$ MeV fm^{-3}) for the MC (the GC), respectively. In all diagrams, the dashed curves correspond to the HS-HS case, the dash-dotted curves to the HS-NS case, and the solid curves to the NS-NS case.

In more detail, for the MDI + APR1 EOS and MC we used the values of (a) $n_{\rm tr} = [0.20, 0.25, 0.30, 0.32, 0.35, 0.38]$ fm^{-3} for the HS-HS case and (b) $n_{\rm tr} = [0.43, 0.50]$ fm^{-3} for the HS-NS case, while for the MDI + APR1 EOS and the GC we used (a) $n_{\rm tr} = [0.20, 0.25, 0.30, 0.32]$ fm^{-3} for the HS-HS case and (b) $n_{\rm tr} = [0.35, 0.38, 0.43]$ fm^{-3} for the HS-NS case. Moving on to the GRDF-DD2 EOS, we notice that for the MC we used (a) $n_{\rm tr} = [0.20, 0.25, 0.30, 0.32]$ fm^{-3} for the HS-HS case and (b) $n_{\rm tr} = [0.35, 0.38]$ fm^{-3} for the HS-NS case, while for the GC we used (a) $n_{\rm tr} = [0.20, 0.25]$ fm^{-3} for the HS-HS case and (b) $n_{\rm tr} = [0.30, 0.32]$ fm^{-3} for the HS-NS case. We remark that even though we kept the region of the component masses identical to the GW170817 observation for the majority of the cases for those hypothetical binary star systems, in some cases we modified and restricted the mass range for computational reasons.

In all cases, the HS-HS case leads to smaller values of Λ, and therefore to a softer EOS, in accordance with the observational data of GW170817. The HS-NS case for a binary star system also lies inside the shaded region provided from LIGO, but in intermediate values of Λ. The NS-NS is the case where the two component stars correspond to the original EOS that we used in each case (the solid black line in the M-R diagrams). As one can observe, the MC provides more cases of the HS-HS scenario than the GC for both EOSs that we used in our study. In addition, the MDI+APR1 EOS for the NS-NS case lies inside the estimation of GW170817 regardless of the combination considered, contrary to the GRDF-DD2 EOS, in which the NS-NS cases lie outside the estimated region.

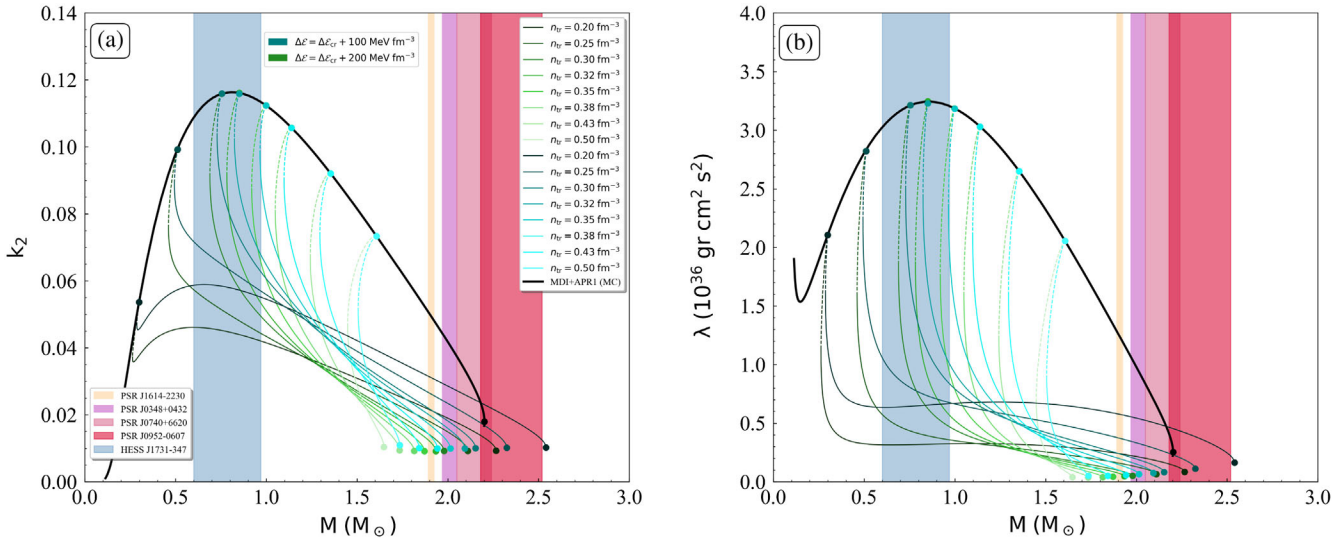

FIG. 5. Tidal parameters (a) k_2 and (b) λ as a relation of the neutron star mass for the MDI+APR1 EOS under the MC and for $\Delta\mathcal{E} = \Delta\mathcal{E}_{\rm cr} + 100$ MeV fm^{-3} (blue curves) and $\Delta\mathcal{E} = \Delta\mathcal{E}_{\rm cr} + 200$ MeV fm^{-3} (green curves). The black curve indicates the original EOS. The dashed part of the curves indicates their unstable region. The shaded regions from left to right represent the HESS J1731-347 remnant [70], PSR J1614-2230 [83], PSR J0348 + 0432 [84], PSR J0740 + 6620 [85], and PSR J0952-0607 [68] pulsar observations for the possible maximum mass.

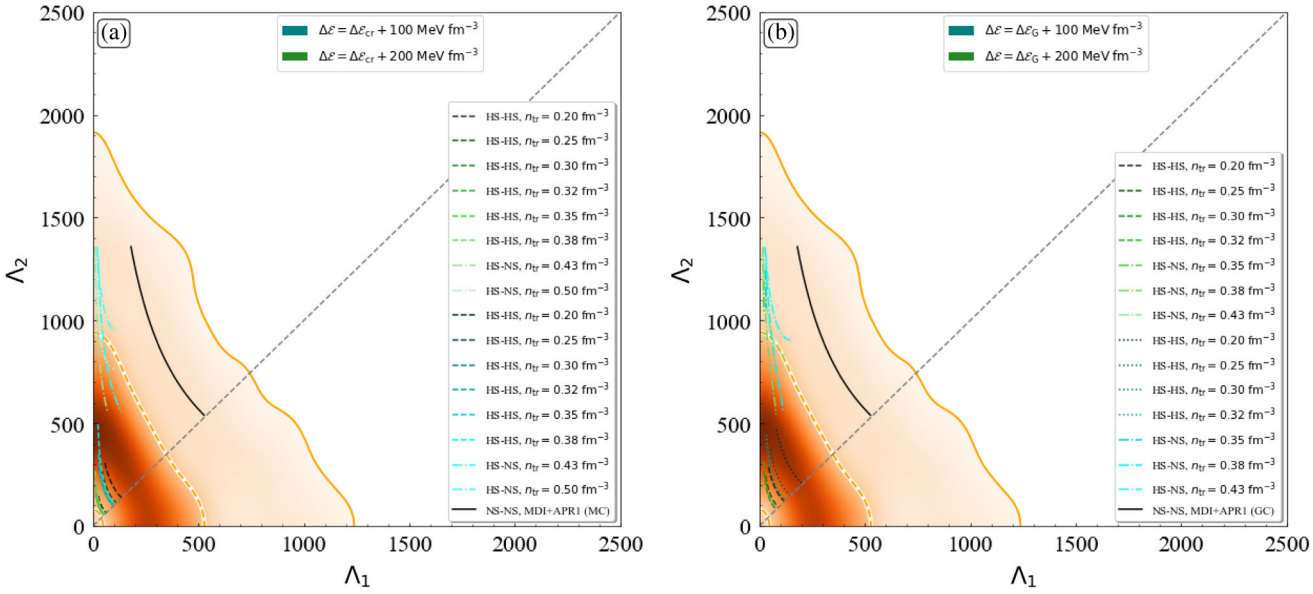

FIG. 6. $\Lambda_1 - \Lambda_2$ relation for the MDI+APR1 EOS and (a) the MC, and (b) the GC. The blue (green) curves correspond to $\Delta\mathcal{E} = \Delta\mathcal{E}_{cr} + 100$ MeV fm^{-3} ($\Delta\mathcal{E} = \Delta\mathcal{E}_{cr} + 200$ MeV fm^{-3}) for the MC, while for the GC the curves correspond to $\Delta\mathcal{E} = \Delta\mathcal{E}_{G} + 100$ MeV fm^{-3} and $\Delta\mathcal{E} = \Delta\mathcal{E}_{G} + 200$ MeV fm^{-3}, respectively. The black curve indicates the original EOS. The shaded region shows the acceptance values derived by the GW170817 event [7].

In Figs. 8 and 9 we show the $\tilde{\Lambda} - q$ relation by using the upper limit on $\tilde{\Lambda}$ provided by the GW170817 event [7]. The curves and colors are the similar to those in the $\Lambda_1 - \Lambda_2$ diagrams. As one can observe, the HS-HS case for both EOSs and constructions lead to much lower values of $\tilde{\Lambda}$. Hence, a possible lower limit on $\tilde{\Lambda}$ would be very useful to restrict the lower values of $\tilde{\Lambda}$, leading to constraints at least in the HS-HS case. Moreover, as we move to higher values of $\Delta\mathcal{E}$, all the curves for both the HS-HS and HS-NS scenarios are shifted to lower values of $\tilde{\Lambda}$, meaning that the increment of $\Delta\mathcal{E}$ has as a result a softer EOS. This behavior was expected if we recall the effect of higher values of $\Delta\mathcal{E}$

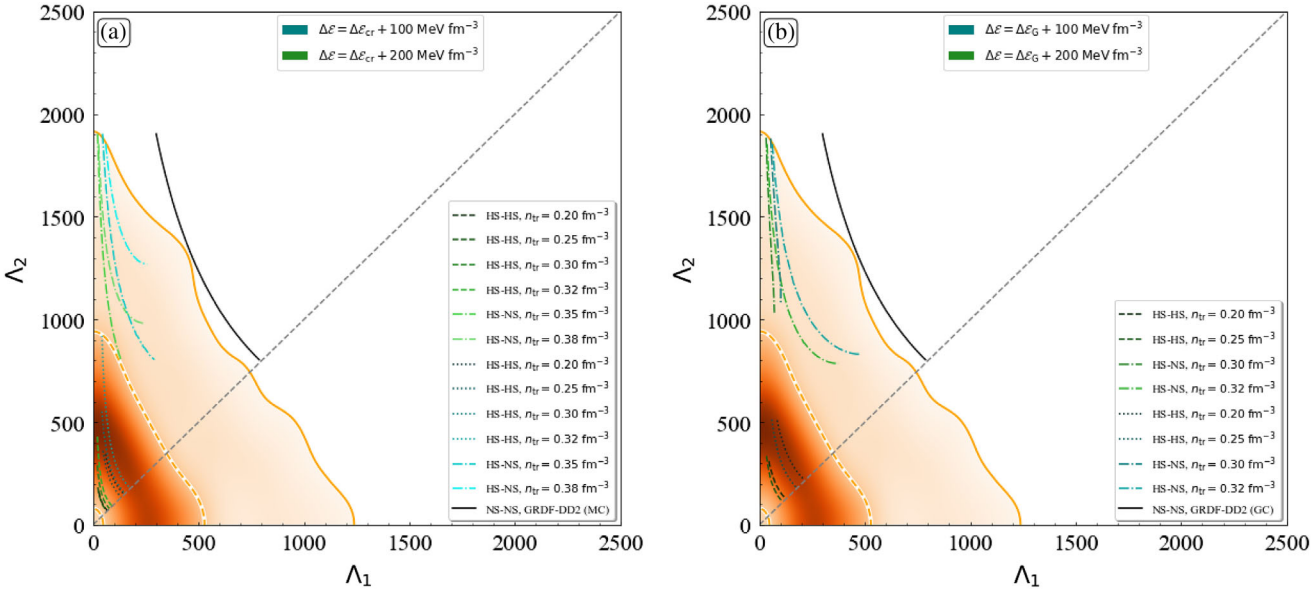

FIG. 7. $\Lambda_1 - \Lambda_2$ relation for the GRDF-DD2 EOS and (a) the MC and (b) the GC. The blue (green) curves correspond to $\Delta\mathcal{E} = \Delta\mathcal{E}_{cr} + 100$ MeV fm^{-3} ($\Delta\mathcal{E} = \Delta\mathcal{E}_{cr} + 200$ MeV fm^{-3}) for the MC, while the curves for the GC correspond to $\Delta\mathcal{E} = \Delta\mathcal{E}_{G} + 100$ MeV fm^{-3} and $\Delta\mathcal{E} = \Delta\mathcal{E}_{G} + 200$ MeV fm^{-3}, respectively. The black curve indicates the original EOS. The shaded region shows the acceptance values derived by the GW170817 event [7].

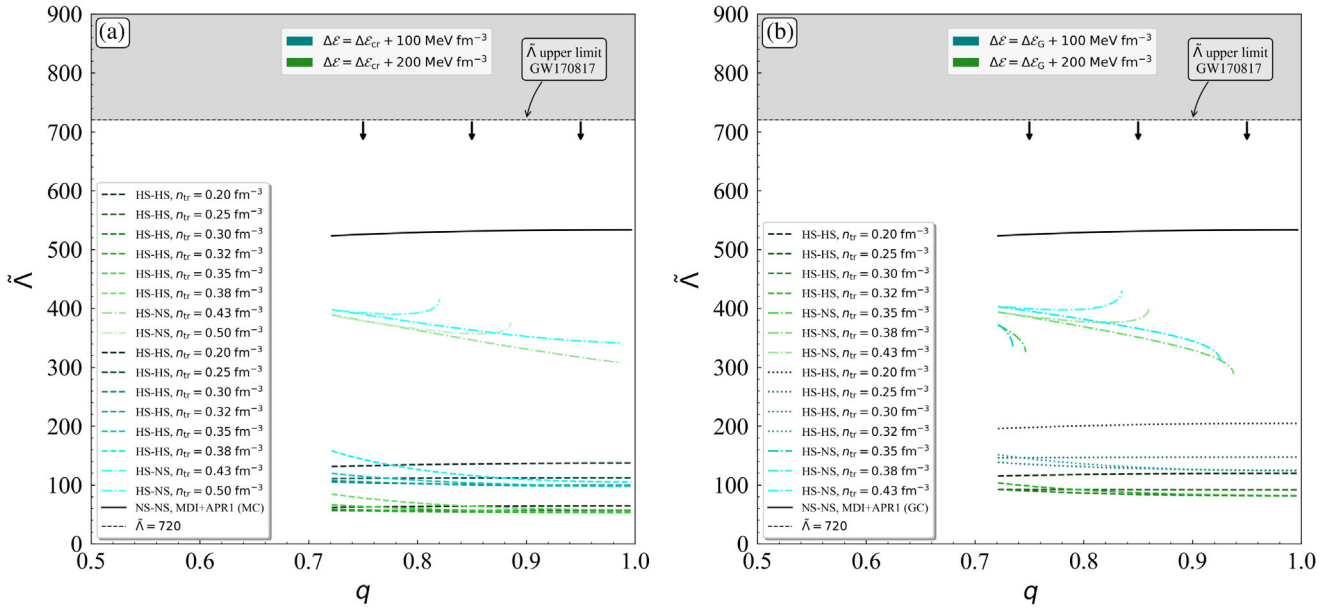

FIG. 8. $\tilde{\Lambda} - q$ relation for the MDI+APR1 EOS and (a) the MC and (b) the GC. The blue (green) curves correspond to $\Delta\mathcal{E} = \Delta\mathcal{E}_{cr} + 100$ MeV fm^{-3} ($\Delta\mathcal{E} = \Delta\mathcal{E}_{cr} + 200$ MeV fm^{-3}) for the MC, while the curves for the GC correspond to $\Delta\mathcal{E} = \Delta\mathcal{E}_{G} + 100$ MeV fm^{-3} and $\Delta\mathcal{E} = \Delta\mathcal{E}_{G} + 200$ MeV fm^{-3}, respectively. The black curve indicates the original EOS. The shaded region shows the acceptance values derived from the GW170817 event [7].

on the EOSs (see the $M - R$ diagrams). Between the two constructions and for both EOSs, the MC provides a higher number of HS-HS cases than the GC. Also, across the same EOS and n_{tr}, the MC leads to lower values of $\tilde{\Lambda}$ than the GC does. Therefore, for low-mass events such as GW170817, the MC is more suitable.

The need for a lower limit on $\tilde{\Lambda}$ than we described before led us to exploit the constrained value of the dimensionless tidal deformability for a single $1.4M_{\odot}$ neutron star derived by the study of the GW170817 event. In Fig. 10 we show the relation between $\Lambda_{1.4}$ and $\Delta\mathcal{E}$. We notice that we used only those values of n_{tr} that provide a separate branch from

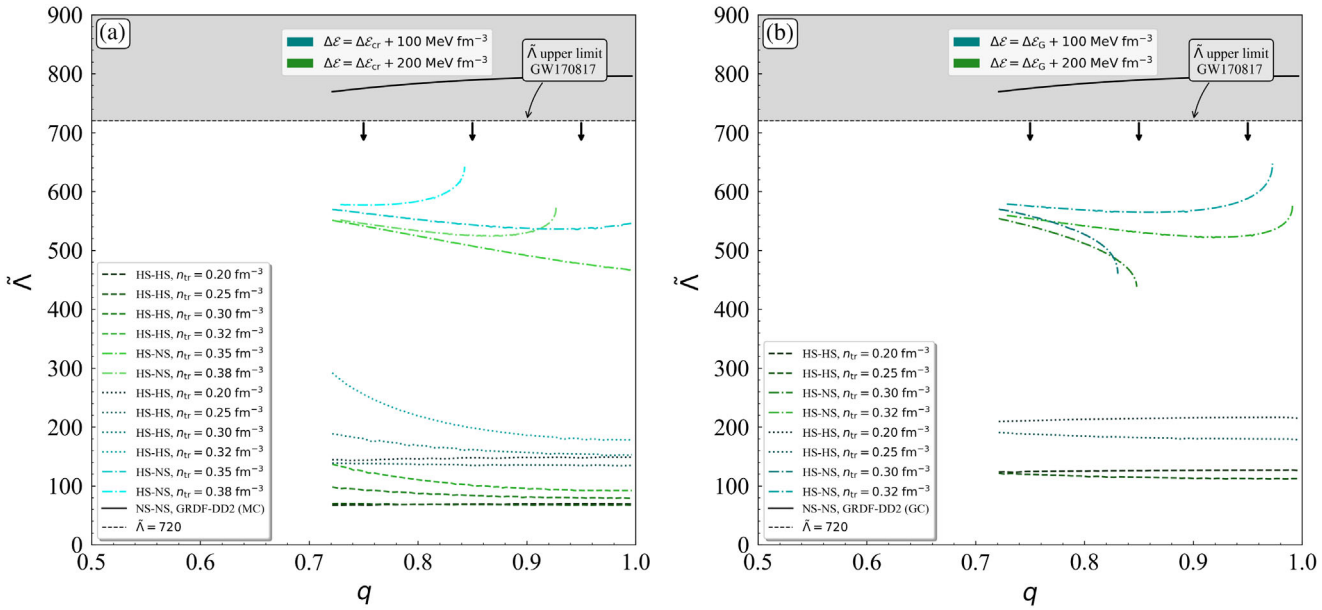

FIG. 9. $\tilde{\Lambda} - q$ relation for the GRDF-DD2 EOS and (a) the MC and (b) the GC. The blue (green) curves correspond to $\Delta\mathcal{E} = \Delta\mathcal{E}_{cr} + 100$ MeV fm^{-3} ($\Delta\mathcal{E} = \Delta\mathcal{E}_{cr} + 200$ MeV fm^{-3}) for the MC, while the curves for the GC correspond to $\Delta\mathcal{E} = \Delta\mathcal{E}_{G} + 100$ MeV fm^{-3} and $\Delta\mathcal{E} = \Delta\mathcal{E}_{G} + 200$ MeV fm^{-3}, respectively. The black curve indicates the original EOS. The shaded region shows the acceptance values derived from the GW170817 event [7].

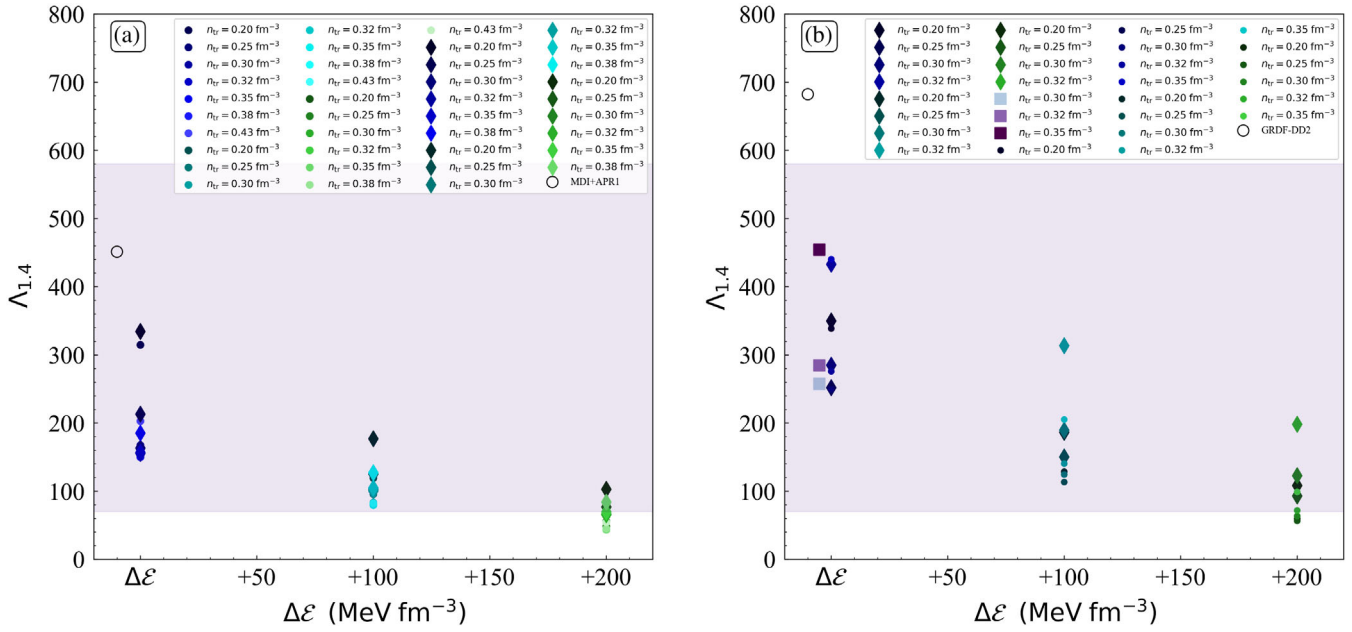

FIG. 10. $\Lambda_{1.4} - \Delta\mathcal{E}$ diagram for a single $1.4M_\odot$ neutron star for (a) the MDI+APR1 and (b) GRDF-DD2 EOS for both the MC (circles) and the GC (diamonds). The squares correspond to the $\Delta\mathcal{E} = \Delta\mathcal{E}_{\rm cr} - 5$ MeV fm^{-3} case under the MC and, for the GRDF-DD2 EOS, the dark blue marks correspond to the $\Delta\mathcal{E}_{\rm cr}$ ($\Delta\mathcal{E}_{\rm G}$) case, the light blue marks correspond to $\Delta\mathcal{E} = \Delta\mathcal{E}_{\rm cr} + 100$ MeV fm^{-3} ($\Delta\mathcal{E} = \Delta\mathcal{E}_{\rm G} + 100$ MeV fm^{-3}), and the green ones correspond to $\Delta\mathcal{E} = \Delta\mathcal{E}_{\rm cr} + 200$ MeV fm^{-3} ($\Delta\mathcal{E} = \Delta\mathcal{E}_{\rm G} + 200$ MeV fm^{-3}) for the MC (the GC). The empty colored circle in each panel indicates the original EOS. The light purple shaded region corresponds to the GW170817 event [6].

the original EOS. As one can observe, as we move from the $\Delta\mathcal{E}_{\rm cr}$ (and $\Delta\mathcal{E}_{\rm G}$ for the GC) to higher values of $\Delta\mathcal{E}$, the variation between the marks decreases. In addition, all the marks that correspond to the GC (diamonds) predict higher values of $\Lambda_{1.4}$ than for the MC for both EOSs. We notice also that there is a violation of the accepted region only for the $\Delta\mathcal{E} = \Delta\mathcal{E}_{cr} + 200$ MeV fm^{-3} and $\Delta\mathcal{E} = \Delta\mathcal{E}_{G} + 200$ MeV fm^{-3}. Moreover, in Fig. 10(b), the squares indicate the $\Delta\mathcal{E} = \Delta\mathcal{E}_{cr} - 5$ MeV fm^{-3} case under MC and for the GRDF-DD2 EOS. As one can observe, as we move to lower values compared to $\Delta\mathcal{E}_{\rm cr}$, the variation increases, which is in accordance with the behavior that we described before.

Furthermore, in order to shed more light on which specific cases should be excluded, we studied the relation between $\Lambda_{1.4}$ and $n_{\rm tr}$. In Fig. 11 we present the aforementioned relation. As a first remark, the MC provides in all cases one more value of $n_{\rm tr}$ than the GC. The GC shifts the curves (dashed) to higher values than the relevant curves of MC (solid). In addition, as we move to higher values of $\Delta\mathcal{E}$, the curves are shifted to lower values of $\Lambda_{1.4}$.

Figure 11(a) corresponds to the MDI + APR1 EOS. The curves that correspond to the $\Delta\mathcal{E}_{\rm cr}$ and $\Delta\mathcal{E} = \Delta\mathcal{E}_{cr} + 100$ MeV fm^{-3} lie inside the estimated region. The same holds for $\Delta\mathcal{E}_{\rm G}$ and $\Delta\mathcal{E} = \Delta\mathcal{E}_{G} + 100$ MeV fm^{-3}. On the other hand, the solid green curve, which corresponds to the MC with $\Delta\mathcal{E} = \Delta\mathcal{E}_{cr} + 200$ MeV fm^{-3}, is excluded. But if we apply the GC, the curve is shifted upward (dashed green curve), with only part lying outside of the estimated region. Specifically, this part is between $n_{\rm tr} = 0.276$ fm^{-3} and $n_{\rm tr} = 0.353$ fm^{-3}. Hence, not only does the kind of construction we choose have a significant role, but the exact value of the transition density affects the final output. Therefore, a further understanding and possible constraints on the transition density $n_{\rm tr}$ are necessary to shed more light on the twin star hypothesis.

Figure 11(b) corresponds to the GRDF-DD2 EOS. The curves that correspond to the $\Delta\mathcal{E}_{\rm cr}$ and $\Delta\mathcal{E} = \Delta\mathcal{E}_{cr} + 100$ MeV fm^{-3} lie inside the estimated region. Only the green solid curve which corresponds to the MC with $\Delta\mathcal{E} = \Delta\mathcal{E}_{cr} + 200$ MeV fm^{-3} lies outside up to $n_{\rm tr} = 0.316$ fm^{-3}, meaning that above this value even this EOS could be acceptable. All the curves that correspond to the GC lie inside the estimated region. As we mentioned above, the construction and the transition density have an important effect on the behavior of the curves. We notice that the purple line indicates the $\Delta\mathcal{E} = \Delta\mathcal{E}_{cr} - 5$ MeV fm^{-3} case under the MC. As we have already noticed, as we move to lower values of $\Delta\mathcal{E}$ than for $\Delta\mathcal{E}_{\rm cr}$, the EOS becomes stiffer; therefore, in this diagram the curve is shifted slightly to higher values of $\Lambda_{1.4}$.

In Fig. 12 we show the M-R diagram for the GRDF-DD2 EOS under the MC and for $\Delta\mathcal{E} = \Delta\mathcal{E}_{\rm cr} - 5$ MeV fm^{-3}, which corresponds to a prediction under the Seidov limit. It is interesting that this case predicts the existence of a second stable branch and, consequently, the existence of a

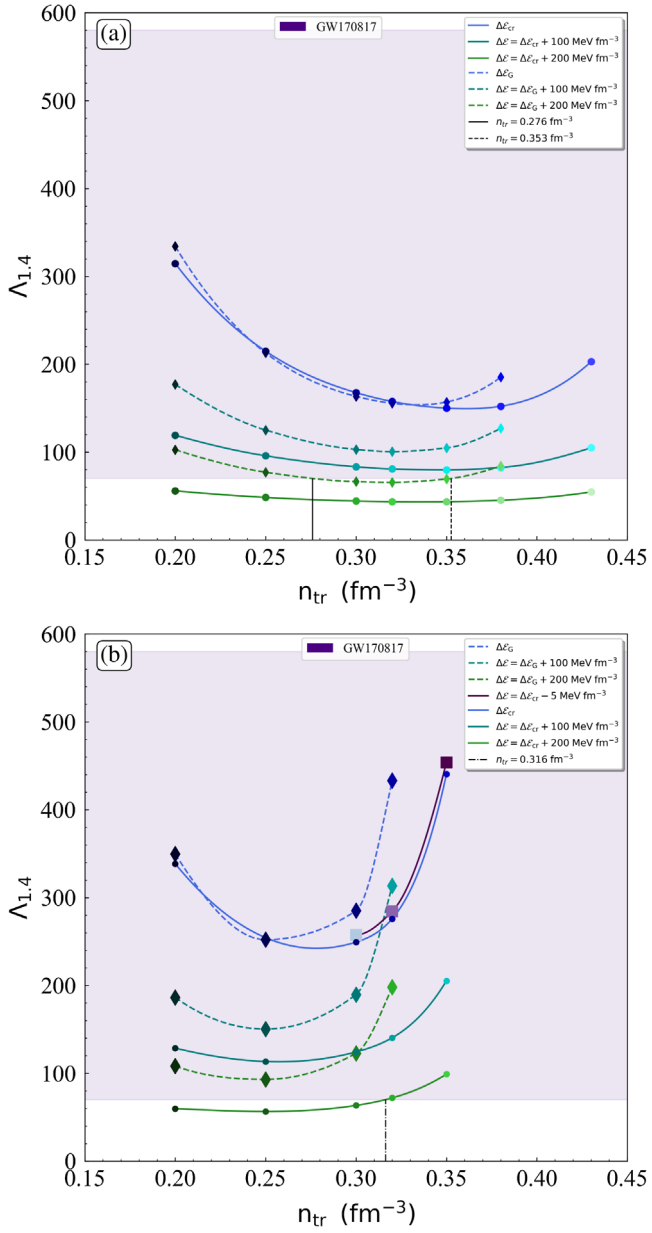

FIG. 11. $\Lambda_{1.4} - n_{tr}$ diagram for a single $1.4M_\odot$ neutron star for (a) the MDI+APR1 and (b) GRDF-DD2 EOS for both the MC (solid lines) and the GC (dashed lines). The dark purple line corresponds to the $\Delta\mathcal{E} = \Delta\mathcal{E}_{cr} - 5$ MeV fm^{-3} case under the MC and, for the GRDF-DD2 EOS, the dark blue lines correspond to the $\Delta\mathcal{E}_{cr}$ ($\Delta\mathcal{E}_G$) case, the light blue lines correspond to $\Delta\mathcal{E} = \Delta\mathcal{E}_{cr} + 100$ MeV fm^{-3} ($\Delta\mathcal{E} = \Delta\mathcal{E}_G + 100$ MeV fm^{-3}), and the green ones correspond to $\Delta\mathcal{E} = \Delta\mathcal{E}_{cr} + 200$ MeV fm^{-3} ($\Delta\mathcal{E} = \Delta\mathcal{E}_G + 200$ MeV fm^{-3}) for the MC (the GC). The light purple shaded region corresponds to the GW170817 event [6].

twin star (and indeed within the predictions of the GW170817 event [7]). However, this case cannot predict the existence of the compact object of the remnant HESS J1731-347 [70]. These results confirm those presented in Figs. 1–4, that is, hybrid EOSs with a large energy density

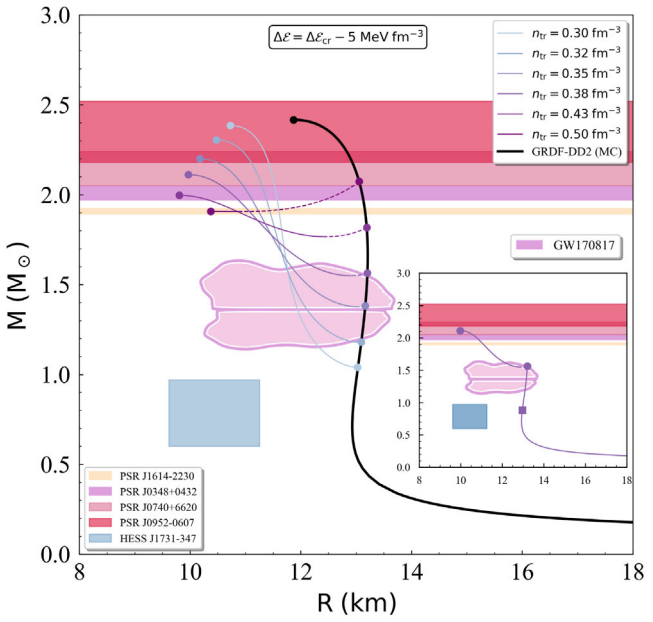

FIG. 12. Mass vs radius for the GRDF-DD2 EOS under the MC and for $\Delta\mathcal{E} = \Delta\mathcal{E}_{cr} - 5$ MeV fm^{-3}. The dashed part of the curves indicates their unstable region. The black curve indicates the original EOS. The shaded regions from bottom to top represent the HESS J1731-347 remnant [70], the GW170817 event [7], PSR J1614-2230 [83], PSR J0348 + 0432 [84], PSR J0740 + 6620 [85], and PSR J0952-0607 [68] pulsar observations for the possible maximum mass. Inset: the case with $n_{tr} = 0.38$ fm^{-3}, where the square represents the phase transition.

gap are preferable for explaining the existence of the above compact object.

C. Rotational frequency at 709 Hz and the PSR J0952-0607 pulsar

The simultaneous observation of mass and frequency of the PSR J0952-0607 pulsar [68] opens a new window for studying the rotating configuration for neutron stars and the possible existence of rotating twin stars. In Figs. 13 and 15 we present three cases of transition density, $n_{tr} = [0.2, 0.25, 0.3]$ fm^{-3}, for both the nonrotation and the rotation in the 709 Hz configuration, with the MC and the GC, respectively. Furthermore, we extended the study to a region of the energy jump, starting from the $\Delta\mathcal{E}_{cr}$ for the MC and $\Delta\mathcal{E}_G$ for the GC and reaching values up to +150 MeV fm^{-3}. In particular, while in Fig. 13(a) there are numerous cases that exist either in the mass limit of the rotating neutron star or in the nonrotating one, there are only three cases where both configurations meet the mass limits simultaneously [68,83–85]. Specifically, (a) $n_{tr} = 0.25$ fm^{-3} and $\Delta\mathcal{E} = \Delta\mathcal{E}_{cr} + 150$ MeV fm^{-3}, (b) $n_{tr} = 0.3$ fm^{-3} and $\Delta\mathcal{E} = \Delta\mathcal{E}_{cr} + 60$ MeV fm^{-3}, and (c) $n_{tr} = 0.3$ fm^{-3} and $\Delta\mathcal{E} = \Delta\mathcal{E}_{cr} + 90$ MeV fm^{-3}. In addition, the aforementioned cases also fulfill the nonrotating radius limit [86], as shown in Fig. 13(b), that is extracted from the GW170817 event [86]

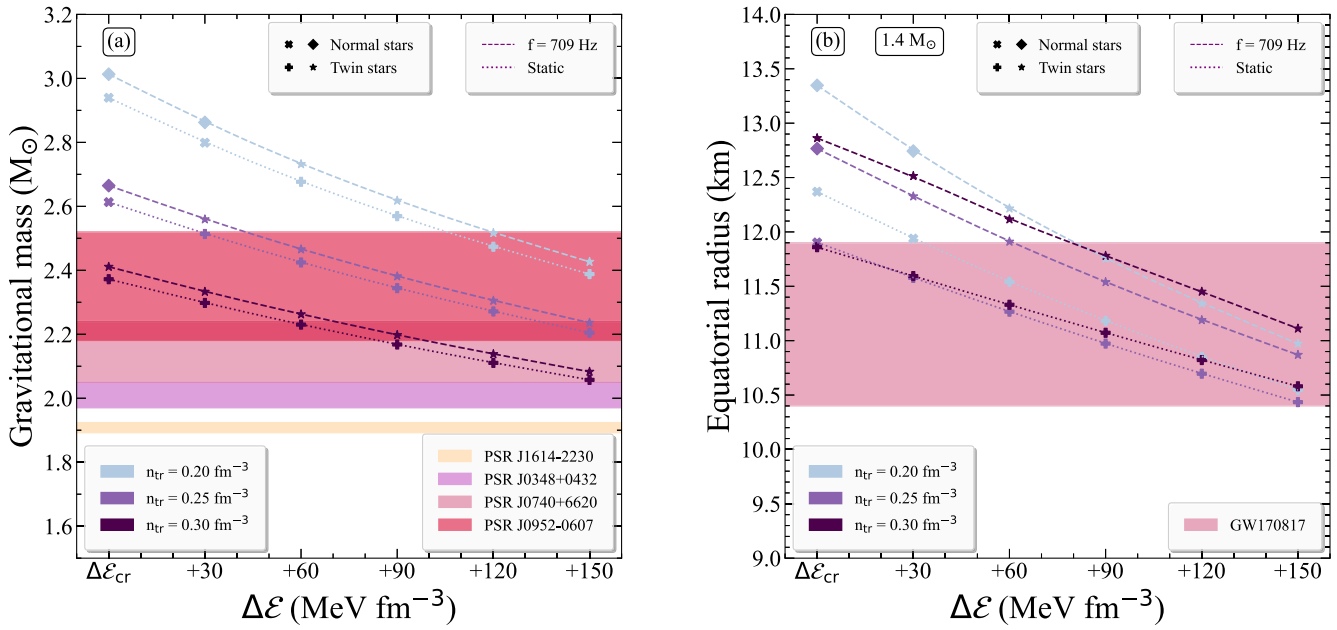

FIG. 13. (a) Gravitational mass as a function of the energy jump for transition densities in the range $[0.2, 0.3]$ fm^{-3} at the maximum mass configuration. The shaded regions from bottom to top represent the PSR J1614-2230 [83], PSR J0348 + 0432 [84], PSR J0740 + 6620 [85], and PSR J0952-0607 [68] pulsar observations for the possible maximum mass. (b) Equatorial radius as a function of the energy jump for transition densities in the range $[0.2, 0.3]$ fm^{-3} at the $1.4M_\odot$ configuration. The shaded region represents the constraints extracted through the GW170817 event [86]. Normal neutron stars are presented with the diamonds and crosses, corresponding to the rotation in the 709 Hz configuration and the nonrotating one, respectively, while twin stars use the stars and plus signs. Both panels correspond to the Maxwell construction method.

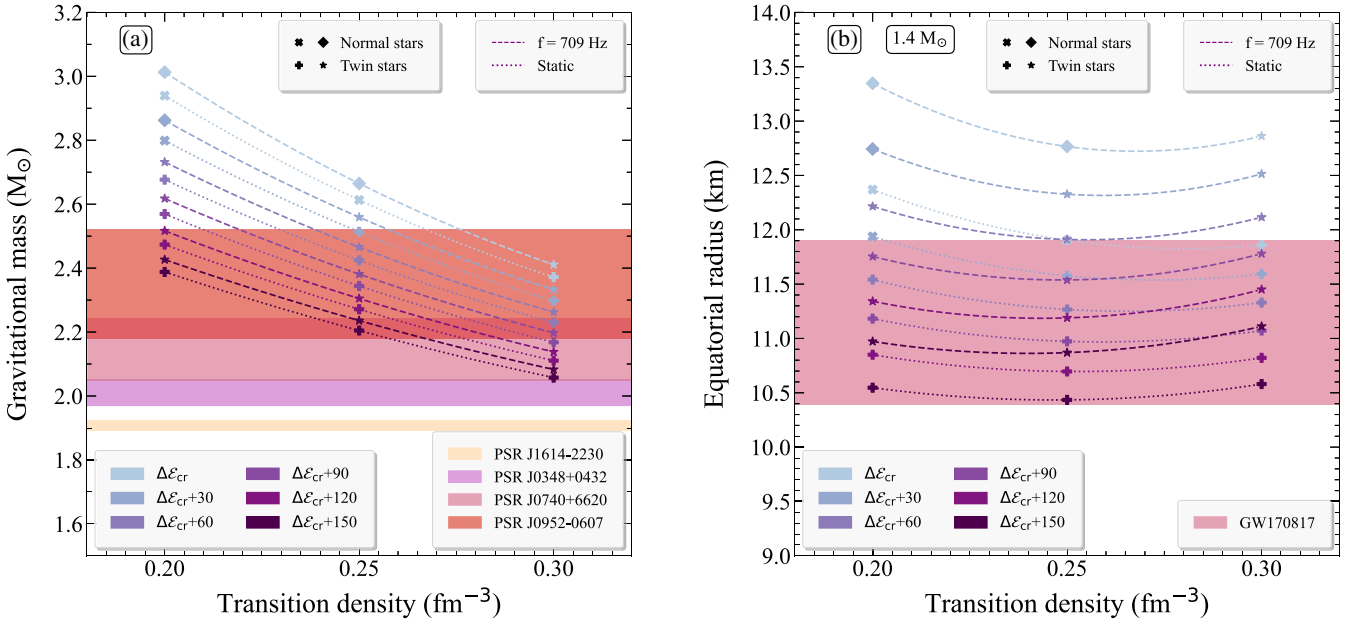

FIG. 14. (a) Gravitational mass as a function of the transition density for energy jumps in the range $[\Delta\mathcal{E}_{cr}, \Delta\mathcal{E}_{cr} + 150]$ MeV fm^{-3} at the maximum mass configuration. The shaded regions from bottom to top represent the PSR J1614-2230 [83], PSR J0348 + 0432 [84], PSR J0740 + 6620 [85], and PSR J0952-0607 [68] pulsar observations for the possible maximum mass. (b) Equatorial radius as a function of the transition density for energy jumps in the range $[\Delta\mathcal{E}_{cr}, \Delta\mathcal{E}_{cr} + 150]$ MeV fm^{-3} in the $1.4M_\odot$ configuration. The shaded region represents the constraints extracted through the GW170817 event [86]. Normal neutron stars are presented with diamonds and crosses corresponding to the rotation in the 709 Hz configuration and the nonrotating one, respectively, while twin stars use the stars and plus signs. Both panels correspond to the Maxwell construction method.

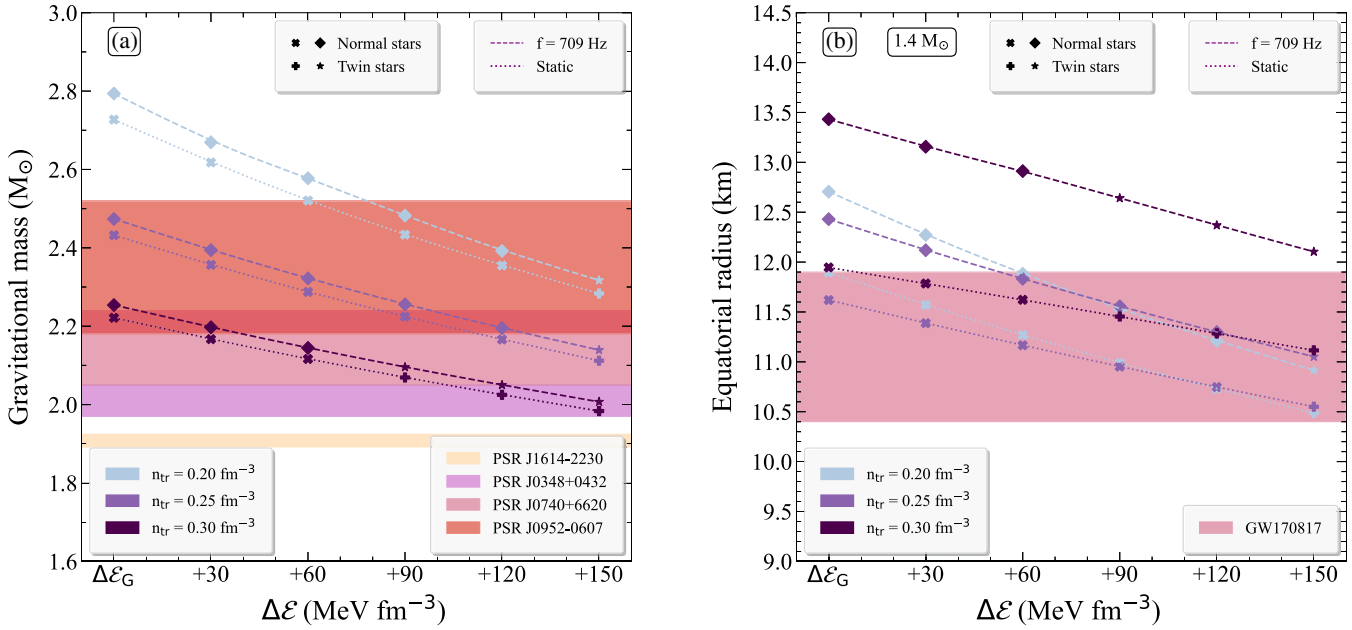

FIG. 15. (a) Gravitational mass as a function of the energy increase for transition densities in the range $[0.2, 0.3]$ fm^{-3} at the maximum mass configuration. The shaded regions from bottom to top represent the PSR J1614-2230 [83], PSR J0348 + 0432 [84], PSR J0740 + 6620 [85], and PSR J0952-0607 [68] pulsar observations for the possible maximum mass. (b) Equatorial radius as a function of the energy increase for transition densities in the range $[0.2, 0.3]$ fm^{-3} at the $1.4M_\odot$ configuration. The shaded region represents the constraints extracted through the GW170817 event [86]. Normal neutron stars are presented with the diamonds and crosses, corresponding to the rotation in the 709 Hz configuration and the nonrotating one, respectively, while twin stars use the stars and plus signs. Both panels correspond to the Gibbs construction method.

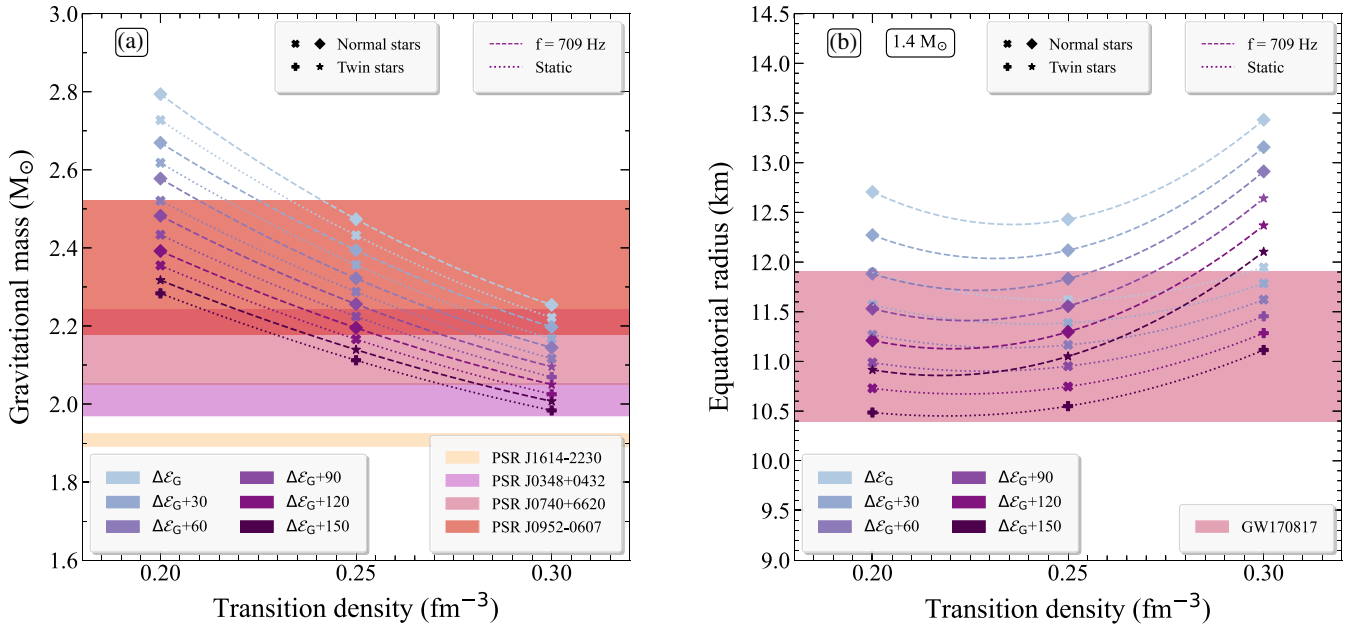

FIG. 16. (a) Gravitational mass as a function of the transition density for energy increases in the range $[\Delta\mathcal{E}_G, \Delta\mathcal{E}_G + 150]$ MeV fm^{-3} at the maximum mass configuration. The shaded regions from bottom to top represent the PSR J1614-2230 [83], PSR J0348 + 0432 [84], PSR J0740 + 6620 [85], and PSR J0952-0607 [68] pulsar observations for the possible maximum mass. (b) Equatorial radius as a function of the transition density for energy increases in the range $[\Delta\mathcal{E}_G, \Delta\mathcal{E}_G + 150]$ MeV fm^{-3} in the $1.4M_\odot$ configuration. The shaded region represents the constraints extracted through GW170817 event [86]. Normal neutron stars are presented with diamonds and crosses corresponding to the rotation in the 709 Hz configuration and the nonrotating one, respectively, while twin stars use the stars and plus signs. Both panels correspond to the Gibbs construction method.

for the $1.4M_\odot$ configuration. In the latter, we also present for completeness and comparison the corresponding radius at 709 Hz. However, in Fig. 13(a), there are numerous cases that can solely describe the 709 Hz configuration. It has to be noted that the aforementioned cases are eligible for the description of the PSR J0952-0607 [68] pulsar since we do not know the corresponding nonrotating limit for the mass. On the contrary, in Fig. 15(a) there are only a few cases that represent twin stars, which nearly all (with one exception) meet the current limits of the gravitational mass only at the nonrotating configuration. In addition, their radius is close to the limits, or even fulfills them for the $1.4M_\odot$ configuration imposed by the GW170817 event, which is indicated in Fig. 15(b). The one exception can describe only the 709 Hz radius at $1.4\,M_\odot$ configuration. We also present the corresponding Figs. 14 and 16, where we highlight the transition density over the energy jump.

The GC configuration presented an effect where, while the nonrotating configuration is not able to produce twin stars, that is not the case at 709 Hz [60]. Specifically, Fig. 17 displays the representative cases: (a) $n_{\rm tr} = 0.25$ fm^{-3} and $\Delta\mathcal{E} = \Delta\mathcal{E}_{\rm G} + 120$ MeV fm^{-3} and (b) $n_{\rm tr} = 0.3$ fm^{-3} and $\Delta\mathcal{E} = \Delta\mathcal{E}_{\rm G} + 60$ MeV fm^{-3}. The last case, $n_{\rm tr} = 0.25$ fm^{-3} and $\Delta\mathcal{E} = \Delta\mathcal{E}_{\rm G} + 90$ MeV fm^{-3}, is not presented so as to preserve the clearness of the figure. Moreover, for clarity, we indicate in the inner part of the figure the region of an EOS at 709 Hz, where the twin star branch appears. Also, we have marked the twin star that corresponds to the first maximum mass configuration along with the relevant radii. This effect added the reported cases in the list where the rotation meets the mass limit of the PSR J0952-0607 pulsar.

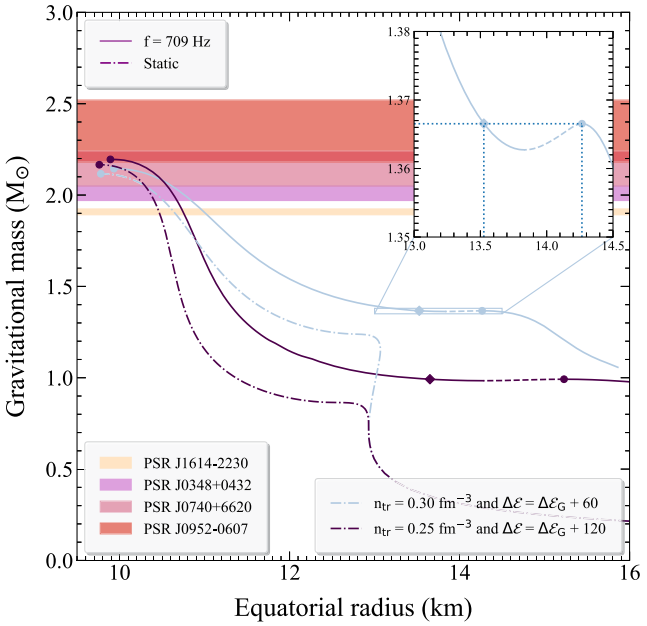

FIG. 17. Gravitational mass as a function of the equatorial radius for two representative cases of the GC: (a) $n_{\rm tr} = 0.25$ fm^{-3} and $\Delta\mathcal{E} = \Delta\mathcal{E}_{\rm G} + 120$ MeV fm^{-3} and (b) $n_{\rm tr} = 0.3$ fm^{-3} and $\Delta\mathcal{E} = \Delta\mathcal{E}_{\rm G} + 60$ MeV fm^{-3}. The circles represent the maximum mass configuration, while the diamonds correspond to the twin stars, assuming a mass equal to the first maximum mass configuration. Inset: twin star branch for the case in which $n_{\rm tr} = 0.3$ fm^{-3} and $\Delta\mathcal{E} = \Delta\mathcal{E}_{\rm G} + 60$ MeV fm^{-3}. The dash-dotted lines represent the nonrotating configuration, while the solid lines correspond to the 709 Hz configuration. As a guide for the eye, the unstable region is marked with dashed lines. The shaded regions from bottom to top represent the PSR J1614-2230 [83], PSR J0348 + 0432 [84], PSR J0740 + 6620 [85], and PSR J0952-0607 [68] pulsar observations for the possible maximum mass.

The MC and GC configurations are both suitable methods to describe twin stars, while the second one, using similar parametrization, is more elaborate. The key differences between them are that (a) the MC provides higher gravitational masses than the GC and (b) the MC rises fairly more twin stars than the GC. A possible explanation for both of them may lie in the existence of the sharp transition and the energy jump applicable on the MC, whereas in the GC both of them are extinct. However, the GC can provide twin stars in the rotating configuration without their appearance in the nonrotating scenario. This peculiar effect may have its origin at the smooth phase transition that the GC uses, alongside the transition density, the rotational frequency, and the hadronic EOS. Nevertheless, a thorough study of the latter effect should be done and will be the subject of a forthcoming paper. An analysis of Figs. 13–17 enriches the scenario of the twin star existence, as they can describe the observed neutron star masses at both nonrotating and rotating configurations. For the numerical integration of the equilibrium equations at the rotating configuration, we used the publicly available numerical code NROTSTAR from the C++ LORENE/NROTSTAR library [87].

V. CONCLUDING REMARKS

The existence of two stable branches in a neutron star configuration, which led to the concept of twin stars, may reveal the scenario of phase transition in the interior of dense nuclear matter. Therefore, it is extremely important to study the above hypothesis from both theoretical and observant points of view. In this work a systematic study concerning the twin star hypothesis has been carried out, and the main conclusions can be summarized as follows.

(1) There could be hybrid or twin star branches that can describe the current observations of binary neutron star systems, such as the GW170817 event. Not only does the transition density play an important role in the possible existence of a twin star branch, but the $\Delta\mathcal{E}$ also affects this scenario. Specifically, as we move to higher values of the $\Delta\mathcal{E}$, it is easier for the twin star branch to exist, even for the lowest values of $n_{\rm tr}$ that we used in our study.

(2) Across the same EOS, the kind of construction that we use affects the behavior of the curves. In general, the MC offers more hybrid and twin star branches in

lower neutron star masses than the GC. Moreover, the MC leads to a softer EOS behavior. Therefore, binary neutron star systems that contain lower component masses (in other words, a lower chirp mass) are better suited to the MC. Also, the GC shifts the curves to higher values of Λ, as one can see in the $\Lambda_{1.4} - n_{\rm tr}$ diagram. This fact has as a consequence that some cases which were to be excluded by using the MC could lie (by using the GC) as a whole or partly inside the estimated area.

(3) In our study we took the observational value of $\tilde{\Lambda}$, using as a reference the GW170817 event. This upper limit was not helpful to further constrain the cases that we studied. On the contrary, because of the fact that the HS-HS binary system scenario has a very soft behavior on the EOS, a possible lower limit on $\tilde{\Lambda}$ could be very helpful to shed more light on the problem, from another point of view. Moreover, a further constraint on the radius (e.g., the radius of a $1.4M_{\odot}$ configuration) could be informative when constraints on the very soft cases are imposed.

(4) The observation of the PSR J0952-0607 pulsar, where both the mass and the frequency are evident, does not exclude the existence of twin stars. In fact, both the MC and the GC provide numerous configurations that can describe solely the rotating configuration, solely the nonrotating configuration, or both of them simultaneously. The latter, since we do not have the corresponding nonrotating mass of the PSR J0952-0607 pulsar, provides us with strong evidence that both static and rotating twin stars can exist.

(5) The rotational frequency in some cases of the GC can introduce twin stars from normal stars. In particular, as the rotating twin star loses its rotational frequency, the neutron star moves to higher energies and stable configurations, where the EOS is more stiff and renders the phenomenon of twin stars extinct. However, an analysis using fixed baryon mass sequences would provide more information on the effect. Nevertheless, we speculate that this effect due to the stiffening of the EOS comes as a consequence to the GC, where a smooth phase transition is employed, in contrast to the MC, where an energy jump appears.

(6) The recent observation of a compact object with the lowest observable mass $M = 0.77^{+0.20}_{-0.17} M_{\odot}$ within the supernova remnant HESS J1731-347 opens a new window to impose constraints on the EOS of dense nuclear matter. In this study, our predictions reinforce the estimation of Doroshenko *et al.* [70] that the observed compact object is a hybrid star with an exotic core rather than the lightest neutron star ever known. This result strengthens the hypothesis of hybrid stars and therefore of the existence of twin stars.

The above conclusions can be summarized as follows: Further systematic theoretical research is required to clarify the role of the method that describes the phase transition in dense nuclear matter, as well as its particular characteristics (density transition, energy, etc.). In addition, more relevant observations from binary neutron star mergers (and more) are necessary to be able to check the plausibility of the theoretical predictions. In this case we will possibly be able to confirm, with sufficient confidence, the existence of twin stars and, even more importantly, to confirm—not only qualitatively but also quantitatively—the phenomenon of phase transition in dense nuclear matter.

ACKNOWLEDGMENTS

The authors would like to thank Professors D. Blaschke, V. Dexheimer, and K. Kokkotas for their useful insights and comments and Dr. S. Typel for the useful discussions and correspondence. The research was supported in part by the Deutsche Forschungsgemeinschaft (DFG) through the cluster of excellence ct.qmat (Exzellenzcluster 2147, Project No. 390858490) and by the Hellenic Foundation for Research and Innovation (HFRI) under the 3rd Call for HFRI Ph.D. Fellowships (Fellowship No. 5657). The implementation of the research was co-financed by Greece and the European Union (European Social Fund-ESF) through the Operational Programme "Human Resources Development, Education and Lifelong Learning" in the context of the Act "Enhancing Human Resources Research Potential by undertaking a Doctoral Research" Sub-action 2: IKY Scholarship Programme for PhD candidates in the Greek Universities.

[1] N. K. Glendenning, *Compact Stars—Nuclear Physics, Particle Physics and General Relativity* (Springer, New York, 1997).

[2] P. Haensel, A. Y. Potekhin, and D. G. Yakovlev, *Neutron Stars 1: Equation of State and Structure* (Springer-Verlag, New York, 2007).

[3] J. Schaffner-Bielich, *Compact Star Physics* (Cambridge University Press, Cambridge, England, 2020).

[4] F. Weber, *Pulsars as Astrophysical Laboratories for Nuclear and Particle Physics* (Institute of Physics, Bristol, England, 1999).

[5] B. P. Abbott *et al.*, Phys. Rev. Lett. **119**, 161101 (2017).

[6] B. P. Abbott *et al.*, Phys. Rev. Lett. **121**, 161101 (2018).
[7] B. P. Abbott *et al.*, Phys. Rev. X **9**, 011001 (2019).
[8] G. Baym, T. Hatsuda, T. Kojo, P. D. Powell, Y. Song, and T. Takatsuka, Rep. Prog. Phys. **81**, 056902 (2018).
[9] M. G. Alford, S. Han, and M. Prakash, Phys. Rev. D **88**, 083013 (2013).
[10] J. E. Christian, A. Zacchi, and J. Schaffner-Bielich, Eur. Phys. J. A **54**, 28 (2018).
[11] G. Montana, L. Tolos, M. Hanauske, and L. Rezzolla, Phys. Rev. D **99**, 103009 (2019).
[12] U. H. Gerlach, Phys. Rev. **172**, 1325 (1968).
[13] B. Kämpfer, J. Phys. A **14**, L471 (1981).
[14] B. Kämpfer, Phys. Lett. **101B**, 366 (1981).
[15] N. K. Glendenning and C. Kettner, Astron. Astrophys. **353**, L9 (2000).
[16] K. Schertler, C. Greiner, J. Schaffner-Bielich, and M. H. Thoma, Nucl. Phys. **A677**, 463 (2000).
[17] D. Blaschke, D. E. Alvarez-Castillo, and S. Benic, *Proc. Sci.*, CPOD2013 (2013) 063 [arXiv:1310.3803].
[18] D. E. Alvarez-Castillo and D. Blaschke, arXiv:1304.7758.
[19] S. Benic, D. Blaschke, D. E. Alvarez-Castillo, T. Fischer, and S. Typel, Astron. Astrophys. **577**, A40 (2015).
[20] D. E. Alvarez-Castillo and D. Blaschke, Phys. Part. Nucl. **46**, 846 (2015).
[21] D. E. Alvarez-Castillo, A. Ayriyan, S. Benic, D. Blaschke. H. Grigorian, and S. Typel, Eur. Phys. J. A **52**, 69 (2016).
[22] A. Ayrinan, N.-U. Bastian, D. Blaschke, H. Grigorian, K. Maslov, and D. N. Voskresensky, Phys. Rev. C **97**, 045802 (2018).
[23] K. Maslov, N. Yasutake, D. Blaschke, A. Ayriyan, H. Grigorian, and T. Maruyama, Phys. Rev. C **100**, 025802 (2019).
[24] D. E. Alvarez-Castillo and D. B. Blaschke, Phys. Rev. C **96**, 045809 (2017).
[25] M. Bejger, D. Blaschke, P. Haensel, J. L. Zdunik, and M. Fortin, Astron. Astrophys. **600**, A39 (2017).
[26] A. Bhattacharyya, I. N. Mishustin, and W. Greiner, J. Phys. G **37**, 025201 (2010).
[27] J. E. Christian, A. Zacchi, and J. Schaffner-Bielich, Phys. Rev. D **99**, 023009 (2019).
[28] J. E. Christian and J. Schaffner-Bielich, Phys. Rev. D **103**, 063042. (2021).
[29] J. E. Christian and J. Schaffner-Bielich, Astrophys. J. **935**, 122 (2022).
[30] S. Han and A. W. Steiner, Phys. Rev. D **99**, 083014 (2019).
[31] P. L. Espino and V. Paschalidis, Phys. Rev. D **105**, 043014 (2022).
[32] H. Tan, T. Dore, V. Dexheimer, J. Noronha-Hostler, and N. Yunes, Phys. Rev. D **105**, 023018 (2022).
[33] J. J. Li, A. Sedrakian, and M. Alford, Phys. Rev. D **104**, L121302 (2021).
[34] Z. Sharifi, M. Bigdeli, and D. Alvarez-Castillo, Phys. Rev. D **103**, 103011 (2021).
[35] E. Benitez, J. Weller, V. Guedes, C. Chirenti, and M. Coleman Miller, Phys. Rev. D **103**, 023007 (2021).
[36] J. J. Li, A. Sedrakian, and M. Alford, Phys. Rev. D **101**, 063022 (2020).
[37] D. E. Alvarez-Castillo, D. B. Blaschke, A. G. Grunfeld, and V. P. Pagura, Phys. Rev. D **99**, 063010 (2019).
[38] V. Paschalidis, K. Yagi, D. Alvarez-Castillo, D. B. Blaschke, and A. Sedrakian, Phys. Rev. D **97**, 084038 (2018).
[39] I. F. Ranea-Sandoval, M. G. Orsaria, S. Han, F. Weber, and W. M. Spinella, Phys. Rev. C **96**, 065807 (2017).
[40] M. Alford and A. Sedrakian, Phys. Rev. Lett. **119**, 161104 (2017).
[41] A. Zacchi, L. Tolos, and J. Schaffner-Bielich, Phys. Rev. D **95**, 103008 (2017).
[42] A. Zacchi, M. Hanauske, and J. Schaffner-Bielich, Phys. Rev. D **93**, 065011 (2016).
[43] A. Bhattacharyya, S. K. Ghosh, M. Hanauske, and S. Raha, Phys. Rev. C **71**, 048801 (2005).
[44] D. Sen, N. Alam, and G. Chaudhuri, Phys. Rev. D **106**, 083008 (2022).
[45] T. Minamikawa, T. Kojo, and M. Harada, Phys. Rev. C **103**, 045205 (2021).
[46] R. De Pietri, A. Drago, A. Feo, G. Pagliara, M. Pasquali, S. Traversi, and G. Wiktorowicz, Astrophys. J. **881**, 122 (2019).
[47] J. L. Zdunik and P. Haensel, Astron. Astrophys. **551**, A61 (2013).
[48] S. Han and M. Prakash, Astrophys. J. **899**, 164 (2020).
[49] A. Li, Z. Y. Zhu, E. P. Zhou, J. M. Dong, J. N. Hu, and C. J. Xia, J. High Energy Astrophys. **28**, 19 (2020).
[50] N. K. Largani, T. Fischer, A. Sedrakian, M. Cierniak, D. E. Alvarez-Castillo, and D. B. Blaschke, Mon. Not. R. Astron. Soc. **515**, 3539 (2022).
[51] O. Ivanytskyi and D. Blaschke, Phys. Rev. D **105**, 114042 (2022).
[52] G. A. Contrera, D. Blaschke, J. P. Carlomagno, A. G. Grunfeld, and S. Liebing, Phys. Rev. C **105**, 045808 (2022).
[53] S. Schramm, V. Dexheimer, and R. Negreiros, Eur. Phys. J. A **52**, 14 (2016).
[54] G. F. Burgio, A. Drago, G. Pagliara, H. J. Schulze, and J. B. Wei, Astrophys. J. **860**, 139 (2018).
[55] M. Sieniawska, W. Turczanski, M. Bejger, and J. L. Zdunik, Astron. Astrophys. **622**, A174 (2019).
[56] E. R. Most, L. R. Weih, L. Rezzolla, and J. Schaffner-Bielich, Phys. Rev. Lett. **120**, 261103 (2018).
[57] R. Nandi and P. Char, Astrophys. J. **857**, 12 (2018).
[58] T. Deloudis, P. Koliogiannis, and Ch. Moustakidis, EPJ Web Conf. **252**, 06001 (2021).
[59] Q. W. Wang, C. Shi, Y. Yan, and H. S. Zong, Nucl. Phys. **A1025**, 122489 (2022).
[60] S. Banik, M. Hanauske, D. Bandyopadhyay, and W. Greiner, Phys. Rev. D **70**, 123004 (2004).
[61] S. Banik and D. Bandyopadhyay, Phys. Rev. C **64**, 055805 (2001).
[62] S. Banik and D. Bandyopadhyay, Phys. Rev. D **67**, 123003 (2003).
[63] P. Haensel, M. Bejger, M. Fortin, and L. Zdunik, Eur. Phys. J. A **52**, 59 (2016).
[64] G. Bozzola, P. L. Espino, C. D. Lewin, and V. Paschalidis, Eur. Phys. J. A **55**, 149 (2019).
[65] J. P. Pereira, M. Bejger, N. Andersson, and F. Gittins, Astrophys. J. **895**, 28 (2020).
[66] S. Han, M. A. A. Mamun, S. Lalit, C. Constantinou, and M. Prakash, Phys. Rev. D **100**, 103022 (2019).
[67] C. G. Bassa, Z. Pleunis, J. W. T. Hessels *et al.*, Astrophys. J. Lett. **846**, L20 (2017).

[68] R. G. Romani, D. Kandel, A. V. Filippenko, T. G. Brink, and W. Zheng, Astrophys. J. Lett. **934**, L17 (2022).
[69] C. Ecker and L. Rezzolla, arXiv:2209.08101.
[70] V. Doroshenko, V. Suleimanov, G. Phlhofer, and Andrea Santangelo, Nat. Astron. **6**, 1444 (2022).
[71] M. Mariani, M. Orsaria, and H. Vucetich, Astron. Astrophys. **601**, A21 (2017).
[72] Ch. Margaritis, P. S. Koliogiannis, and Ch. C. Moustakidis, Phys. Rev. D **101**, 043023 (2020).
[73] A. Kanakis-Pegios, P. S. Koliogiannis, and Ch. C. Moustakidis, Phys. Rev. C **102**, 055801 (2020).
[74] P. S. Koliogiannis, A. Kanakis-Pegios, and Ch. C. Moustakidis, Found. Phys. **1**, 217 (2021).
[75] Z. F. Seidov, Sov. Astron. **15**, 347 (1971).
[76] J. M. Lighthill, Mon. Not. R. Astron. Soc. **110**, 339 (1950).
[77] S. Postnikov, M. Prakash, and J. M. Lattimer, Phys. Rev. D **82**, 024016 (2010).
[78] E. E. Flanagan and T. Hinderer, Phys. Rev. D **77**, 021502(R) (2008).
[79] T. Hinderer, Astrophys. J. **677**, 1216 (2008).
[80] T. Hinderer, B. D. Lackey, R. N. Lang, and J. S. Read, Phys. Rev. D **81**, 123016 (2010).
[81] P. S. Koliogiannis and Ch. C. Moustakidis, Astrophys. J. **912**, 69 (2021).
[82] S. Typel, J. Phys. G **45**, 114001 (2018).
[83] Z. Arzoumanian, A. Brazier, S. Burke-Spolaor *et al.*, Astrophys. J. Suppl. Ser. **235**, 37 (2018).
[84] J. Antoniadis, P. Freire, N. Wex *et al.*, Science **340**, 448 (2013).
[85] H. Cromartie, E. Fonseca, S. Ransom *et al.*, Nat. Astron. **4**, 72 (2020).
[86] C. D. Capano, I. Tews, S. M. Brown, B. Margalit, S. De, S. Kumar, D. A. Brown, B. Krishnan, and S. Reddy, Nat. Astron. **4**, 625 (2020).
[87] Computer code LORENE, http://lorene.obspm.fr/, 1998.